

Microlensing constraint on Primordial Black Hole abundance with Subaru Hyper Suprime-Cam observations of Andromeda

Sunao Sugiyama,^{1,*} Masahiro Takada,^{1,2} Naoki Yasuda,^{1,2} and Nozomu Tominaga^{3,4,5}

¹*Kavli Institute for the Physics and Mathematics of the Universe (WPI),
The University of Tokyo Institutes for Advanced Study (UTIAS),
The University of Tokyo, Chiba 277-8583, Japan*

²*Center for Data-Driven Discovery (CD3), Kavli IPMU (WPI),
UTIAS, The University of Tokyo, Kashiwa, Chiba 277-8583, Japan*

³*National Astronomical Observatory of Japan, 2-21-1 Osawa, Mitaka, Tokyo 181-8588, Japan*

⁴*Astronomical Science Program, The Graduate University for Advanced
Studies (SOKENDAI), 2-21-1 Osawa, Mitaka, Tokyo 181-8588, Japan*

⁵*Department of Physics, Konan University, 8-9-1 Okamoto, Kobe, Hyogo 658-8501, Japan*

(Dated: February 6, 2026)

We present updated microlensing analysis results based on high-cadence (~ 2 min) Subaru Hyper Suprime-Cam (HSC) observations of the Andromeda Galaxy (M31) in 2014, 2017, and 2020, yielding a total of 39.3 hours of data. We use a point-lens finite-source model for the microlensing light curve model and employ multi-stage selection procedures to identify microlensing candidates. From more than 25,000 variable candidates detected across all nights, we identify 12 microlensing candidates with light-curve timescales shorter than 5 hours, and among them, 4 secure candidates with high-significance detections. We estimate detection efficiencies using light-curve-level simulations that account for observational conditions and finite-source effects. Using a hierarchical Bayesian framework that combines the light-curve fitting information for each candidate with the Poisson statistics of the number of candidates, we derive constraints on parameters that characterize the abundance and mass scale of primordial black hole (PBH) dark matter. First, we derive upper limits on the PBH abundance under the null hypothesis that all events are assumed to be false detections. Next, employing the PBH hypothesis in which all (or only secure) candidates are assumed to be due to PBH microlensing, we derive the allowed region of the PBH parameters; the inferred mass scale is $M_{\text{PBH}} \sim 10^{-7}\text{--}10^{-6} M_{\odot}$, and the PBH abundance to the total dark matter is $f_{\text{PBH}} \sim \mathcal{O}(10^{-2}\text{--}10^{-1})$. Our results demonstrate that HSC-M31 monitoring remains a uniquely powerful probe of PBHs, and highlight the need for further studies for example, using Rubin Observatory LSST observations of the Large Magellanic Cloud.

I. INTRODUCTION

Gravitational microlensing is a phenomenon in which the apparent brightness of a background star is temporarily amplified by the gravitational field of a compact object passing close to the line of sight to the star [1, 2]. The characteristic timescale and magnification of a microlensing event are determined primarily by the mass of the lens and its relative transverse velocity with respect to the source and the observer. Because microlensing does not rely on the luminosity of the lens, it provides a unique and powerful probe of otherwise invisible compact objects.

Microlensing surveys have been extensively used to detect and characterize exoplanets, and forthcoming wide-field, high-cadence surveys such as the Roman Space Telescope [3, 4] and the Vera C. Rubin Observatory (LSST) [5, 6] are expected to substantially advance our understanding of planetary populations through this technique. Beyond exoplanet science, microlensing has also been widely applied to the study of non-luminous compact objects, including candidates for dark matter.

Primordial black holes (PBHs) are a particularly compelling dark matter candidate. They may have formed in the early Universe from the collapse of primordial density fluctuations [7–9] and could contribute a non-negligible fraction of the present-day dark matter density [e.g., 10, 11]. Constraining the PBH abundance, commonly parameterized by their fraction of the dark matter, requires statistically robust analyses of microlensing event rates across a wide range of timescales.

Early microlensing searches for compact dark matter objects were carried out by the MACHO and EROS collaborations, establishing foundational methodologies for subsequent studies stellar-mass range [e.g., 12, 13]. Subsequent long-timescale microlensing surveys by OGLE further tightened these constraints using large samples of events toward the Galactic bulge [14, 15]. Later surveys, including OGLE [16] and MOA [17], have reported large samples of microlensing events, some of which exhibit light curves with timescales shorter than a day indicating isolated low-mass lenses such as free-floating planets (FFPs) [18, 19]. However, observations toward the Galactic bulge may suffer from significant contamination by FFPs, if the microlensing data are used to search for PBHs.

A very recent high-cadence microlensing experiment by the OGLE collaboration has provided updated con-

* sunaosugiyama@gmail.com

straints on primordial black holes in the sub-solar mass regime [20]. In this study, two short-timescale candidate events were identified; however, detailed analyses suggested that one event is likely associated with a nearby dwarf star, while the other is consistent with a disk lens. Based on the interpretation that no convincing PBH microlensing event was detected, the authors derived upper limits on the PBH dark matter fraction over the mass range from $M \sim 10^{-7} M_{\odot}$ to $1, M_{\odot}$, with the strongest constraint of $f_{\text{PBH}} \lesssim 10^{-3}$ at $M \sim 10^{-6} M_{\odot}$. These results demonstrate the strong potential of high-cadence microlensing surveys. At the same time, it is useful to obtain complementary constraints using independent instruments, analysis pipelines, and different target fields and lines of sight, in order to further strengthen the overall picture of PBH abundance inferred from microlensing observations.

Observations of the Andromeda Galaxy (M31) offer a complementary and advantageous approach. The Subaru Telescope’s Hyper Suprime-Cam (HSC) [21–24] combines a large 8.2-meter aperture with excellent image quality and an exceptionally wide field of view, enabling simultaneous monitoring of a vast number of unresolved stars in M31 with high cadence. In particular, the 1.5-degree diameter field of view of HSC closely matches the angular extent of M31, maximizing sensitivity to microlensing events caused by lenses lying in the Galactic and M31 halos.

Using a single night of HSC observations in 2014, Niikura *et al.* [25] placed stringent constraints on the abundance of PBHs over a wide mass range, demonstrating the exceptional power of this dataset. Despite the strength of these constraints, only one candidate microlensing event was identified, highlighting the importance of further analyses with expanded datasets and improved modeling techniques.

The HSC observations, characterized by short exposure times (90 seconds) and high cadence, are particularly well suited for detecting microlensing events caused by low-mass PBHs, which are expected to produce very short-duration signals. Moreover, the halo-dominated line of sight toward M31 significantly reduces contamination from FFPs compared to Galactic bulge surveys, enhancing the reliability of PBH searches [26, 27].

Recent developments in microlensing analysis, especially the incorporation of finite-source effects [28, 29], provide additional opportunities to improve sensitivity to short-timescale events. While the standard Paczyński light curve assumes a point-like source, real stars have finite angular sizes, which can substantially modify the magnification profile, particularly for small Einstein radii or close lens–source alignments. Finite-source modeling, typically implemented by convolving the point-source magnification with the surface brightness profile of the source star, enables more accurate characterization and selection of microlensing events.

In this paper, we present a comprehensive reanalysis of the 2014 HSC dataset and incorporate additional ob-

TABLE I. Summary of the HSC datasets used in this paper. The first column lists the observing date. The second column denotes the PI of the observation. The third column denotes the number of allocated nights for each run. The fourth column denotes the filters used in each observation. The fifth column denotes the number of exposures taken on each observing date. The sixth column, denotes as T_{eff} (in units of hours), indicates the effective duration of the observation. Here the duration accounts for the period when the observation was halted due to focusing or bad weather conditions such as high humidity. The last column, denoted as “PSF”, indicates the typical seeing size.

Date	PI	Nights	Filter	Images	T_{eff}	PSF
2014-11-24	Takada	1.0	<i>r</i>	189	6.4	0.68''
2017-09-20	Takada	1.0	<i>r2</i>	215	7.1	0.86''
2020-10-21	Sugiyama	0.5	<i>r2</i>	152	5.0	0.80''
2020-10-22	Sugiyama	0.5	<i>r2</i>	156	5.2	0.84''
2020-11-11	Sugiyama	0.5	<i>r2</i>	56	1.8	1.13''
2020-11-12	Sugiyama	0.5	<i>r2</i>	126	4.1	1.38''
2020-11-14	Sugiyama	0.5	<i>r2</i>	152	5.1	0.80''
2020-11-16	Sugiyama	0.5	<i>r2</i>	0	0.0	—
2020-11-18	Sugiyama	0.5	<i>r2</i>	34	0.0	—
2020-11-20	Sugiyama	0.5	<i>r2</i>	140	4.6	1.08''

servations obtained in 2017 and 2020. By expanding the temporal baseline and applying refined event selection and modeling techniques, we aim to improve constraints on the PBH abundance and to establish a robust framework for interpreting microlensing events in the context of dark matter studies.

This paper is organized as follows. In Section II, we describe the Subaru HSC observations of the Andromeda Galaxy and summarize the datasets used in this analysis. Section III details the data reduction procedures and the multi-stage event selection pipeline employed to identify microlensing candidates. In Section IV, we present our characterization of the detection efficiency based on light-curve-level simulations. Section V introduces the likelihood framework and the hierarchical Bayesian methodology used to infer the parameters of the primordial black hole population. The resulting constraints on the primordial black hole abundance and mass scale are presented in Section VI. Finally, we discuss the implications of our results and future prospects in Section VII.

II. DATA

We carried out a series of monitoring observations of stars in Andromeda Galaxy (M31), as summarized in Table I. The first observation was carried out on November 24, 2014. One night was allocated for this observation and 189 images were obtained, each of which has an exposure of 90 seconds and a read out of 30 seconds, resulting in 2-minute cadence. Excluding data affected by bad weather and other overheads, the effective science-quality observing time for this night amounts to a total of 6.4 hours. The typical seeing size is 0.68''. The *r*-band

TABLE II. Summary of the master catalog of variable-star candidates.

Name of Master catalog	Number of events
2014-11-24	7281
2017-09-20	6199
2020-10-21	3636
2020-10-22	1582
2020-11-11	348
2020-11-12	2029
2020-11-14	2504
2020-11-16	0
2020-11-18	0
2020-11-20	1714

filter was replaced with a new one ($r2$) on July 28, 2016 (HST), and all our observations after 2017-09-20 were conducted using the $r2$ filter [30].

The second observation was carried out on September 20, 2017. We obtained 215 images with a total effective observing time of $T_{\text{eff}} = 7.1$ hours, under typical seeing conditions of $0.86''$.

The other eight observations were carried out in 2020. In this set of observations, 8 half-nights were allocated, yielding a net total of 4 full nights. We obtained science-quality data on November 12, 14 and 20 and partially on November 11, while the data collected on November 16 and 18 did not meet the expected quality due to poor weather conditions. In total, we use 39.3 hours of HSC data in this paper.

III. DATA ANALYSIS

A. Standard image processing

As a first step of the data analysis, we performed the standard image processing using the HSC pipeline [31], which is a dedicated data reduction pipeline for HSC imaging data. We used the latest version `hscpipe8` in this paper, while Niikura *et al.* [25] used `hscpipe3`. The standard image processing includes a series of image calibrations; bias subtraction, flat fielding with dome flats, coadding, astrometry and photometry calibrations. We refer the readers to Aihara *et al.* [32] for detail of `hscpipe8`.

B. Image subtraction and object detection

Since M31 is a dense stellar field and our microlensing analysis lies in the pixel lensing regime, we need to employ the difference image technique to detect variable candidates in the images [33]. The difference image is developed in Alard and Lupton [34], Alard [35], and has been implemented in `hscpipe8`.

As we are interested in microlensing events on timescales within a single night, we performed the image

subtraction for the HSC data taken during each night listed in Table I. First, we co-added the 10 images with the best seeing conditions to create a reference image for each night. Fig. 1 shows the PSF size as a function of the elapsed time since the start of the observations for each night. The seeing was good in the 2014-11-24 data, and the 10 images used to generate the reference image have a mean seeing size of $0.47''$. For the 2017-09-20, 2020-10-21, and 2020-10-22 data, the seeing was overall good, and the 10 images used to generate the reference image have mean seeing sizes of $0.59''$ – $0.62''$ for each night. For the 2020-11-14 data, the seeing was stable throughout the observing hours, and the 10 images used for the reference image have a mean seeing size of $0.68''$, which is worse than those on the aforementioned dates. For the 2020-11-11, 2020-11-12 and 2020-11-20 data, the seeing was poor, and the data are not usable for the microlensing analysis, as we will show below. In particular we were not able to generate a useful reference image for the 2020-11-12 data.

Next, we co-added three consecutive images to generate a target image at each epoch. Finally, we subtracted the reference image from each target image to produce a difference image, from which we detected variable object candidates. Here we defined variable candidates as local minima or maxima in each of the difference images. To obtain a reliable catalog of variable candidates, we applied the following selection criteria:

- PSF magnitude cut: A candidate must have 5σ or higher PSF magnitude in at least two difference images. The candidates in different difference images are identified as the same object when their positions is within 2 pixels of each other.
- Size cut: The size of a candidate should be consistent with the PSF size within 25%.
- Roundness cut: Candidates should have a round shape, requiring the axis ratio of the object to be greater than 0.75, as the HSC PSF is nearly round.
- Shape cut: Candidates are required to have a shape consistent with PSF; specifically, the residual image, obtained by subtracting a rescaled PSF from the difference image, must have a cumulative residual smaller than 3σ .

These selection criteria yield reliable candidate objects, which we refer to as the master catalog for the data of each observation date. The number of the objects in each master catalog are summarized in Table II.

Once we obtained the master catalog for a given observation night, we measured the forced photometry for each candidate on each exposure image of that night, at the position where the object was detected. For the photometry error at each epoch, we use the variance of the photometry measurements at 1,000 random points in the corresponding patch, following the method in Ref. [25]. The error estimated in this way includes the large-scale

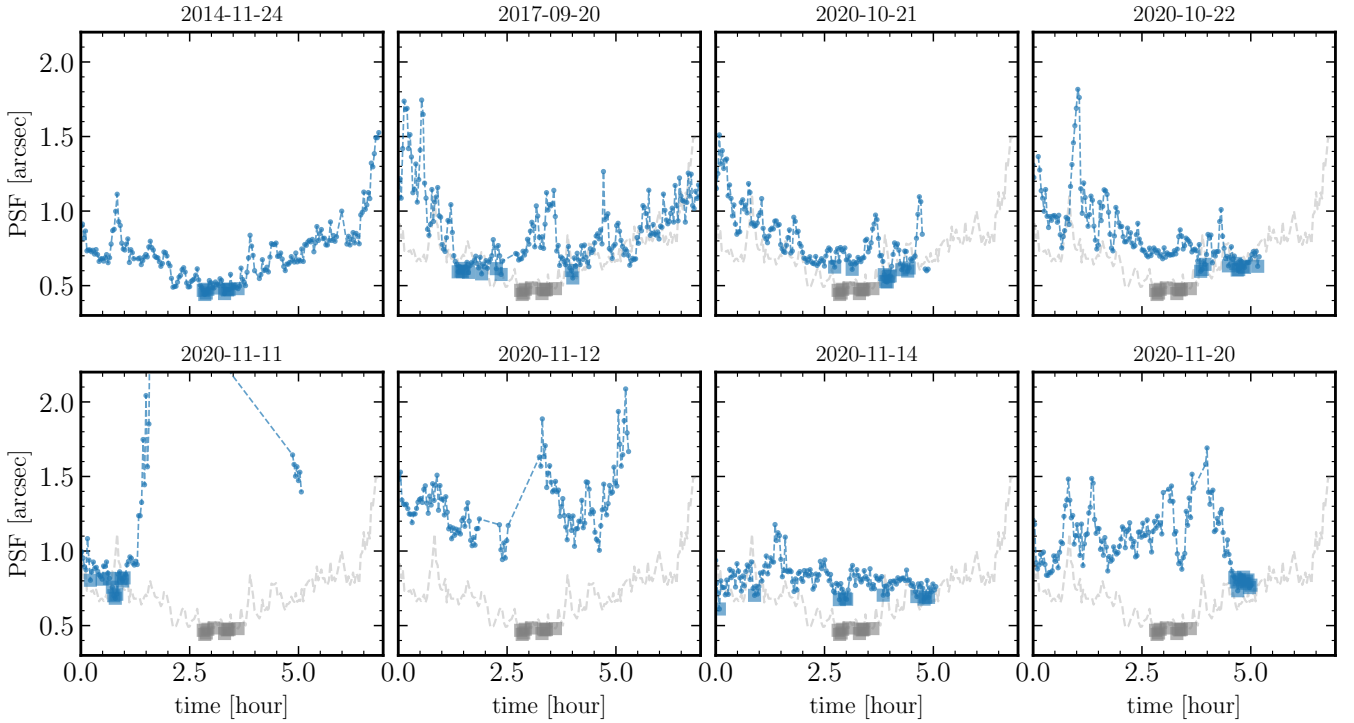


FIG. 1. In each panel, the solid line indicates the PSF size (seeing) as a function of the observation time from the beginning of observation on each night, and the square points indicate the 10 images with the best seeing on each night, which are therefore used to generate the reference images for image subtraction, as described in Section III B. The PSF size of the 2014-11-24 data is overplotted in gray in each panel for comparison. Note that the 2020-11-12 data have relatively large seeing compared to other observation nights, and therefore we do not generate a reference image for this night. We also note that, although the 2020-11-14 data are under good conditions throughout the night, the reference image was generated from images with relatively large seeing compared to those from the 2014-11-24 and 2017-09-20 data, which are the best data in our dataset.

residual background arising from imperfect background subtraction.

C. Event Selection

Our selection process of microlensing events consists of three levels. The first-level selection is the light-curve based selection, where the selection is applied to the derived summary statistics of each light curve. The second-level selection is based on the images to visually assess if the events are really likely due to microlensing or merely imposters. The third-level selection is based on the light curves and images taken in other observing dates at the detection sky position. This ensures that the selected events are not repeating variables.

We start with the first-level selection. In what follows, we denote the flux in the difference image as ΔF_i , where the subscript i refers to the i -th image in the light curve of a given candidate.

Since the light curve of a microlensing event has a peak at the time of the closest approach between the lens and the source on the sky, we first select candidates whose light curves exhibit a peak. For this purpose, we define a

bump in each light curve as a time interval during which the difference flux is consecutively above the mean difference flux

$$\Delta F_i - \overline{\Delta F} > 2\sigma(\Delta F_i). \quad (1)$$

Here, the mean difference flux $\overline{\Delta F}$ is defined as the average over all the time indices. Note that a single light curve may have multiple bumps. Then we define the length of a bump in a light curve, denoted as `bump`, by the number of images within the bump. If a light curve has multiple bumps, we define `bump` as the largest `bump` among them. If a light-curve has no bump, we set `bump` = 0. The first selection criterion is based on the bump length, requiring `bump` ≥ 3 . For the later use, we also define the most significant bump as the one with the highest bump significance:

$$\text{bumpsignif} = \sum_{i \in \text{bump}} \delta \Delta F_i. \quad (2)$$

Using the start and end times for the most significant bump, denoted as $t_{\text{start}}^{\text{bump}}$ and $t_{\text{end}}^{\text{bump}}$, we define a rough estimate of the peak time as $t_{0,\text{bump}} = (t_{\text{end}}^{\text{bump}} + t_{\text{start}}^{\text{bump}})/2$ and its uncertainty as $\sigma(t_0^{\text{bump}}) = (t_{\text{end}}^{\text{bump}} - t_{\text{start}}^{\text{bump}})/2 + \Delta t$, where

TABLE III. Summary statistics of each candidate for selection. See Section III C for the details.

Name	Definition
<code>bump</code>	The time interval during which $\Delta F_i - \Delta \bar{F} > 2\sigma(\Delta F_i)$, being satisfied consecutively over a time interval
<code>bumplen</code>	The duration or the number of images of the longest bump
t_{FWHM}	The FWHM time interval computed from the best-fit microlensing light-curve model
<code>mlc2</code>	The chi-square value of the best-fit microlensing light-curve model, integrated over the fitting time interval
<code>mlc2i</code>	Same as <code>mlc2</code> , but using only the images with $ t_i - t_0 < t_{\text{FWHM}}$
<code>mlc2o</code>	Same as <code>mlc2</code> , but using only the images with $ t_i - t_0 > t_{\text{FWHM}}$
<code>mlc2il</code>	Same as <code>mlc2i</code> , but using only the images before the peak time
<code>mlc2ir</code>	Same as <code>mlc2i</code> , but using only the images after the peak time
<code>mlc2ol</code>	Same as <code>mlc2o</code> , but using only the images before the peak time
<code>mlc2or</code>	Same as <code>mlc2o</code> , but using only the images after the peak time
<code>asym</code>	Asymmetry parameter of the light curve, as defined in Eq. (8)
<code>scorr</code>	The cross-correlation between ΔF and the seeing size at each epoch, as defined in Eq. (9)
<code>scorrs</code>	The cross-correlation between ΔF and the seeing size for a certain time interval (see text for the details)
<code>max A</code>	The maximum magnification predicted by the best-fit microlensing model
<code>mlsig</code>	The significance of the peak detection as a micro-lensing light-curve event, as defined in Eq. (10)

TABLE IV. Selection criteria for microlensing candidates. See Section III C for the details.

Level	Label	Criterion	Purpose
1	<code>bump</code>	<code>bumplen</code> ≥ 3.0	a light-curve peak spanning at least three consecutive detected data points
1	<code>mlc2</code>	$\text{mlc2} \leq 3.0$	a reasonable goodness-of-fit to a microlensing model
1	<code>mlc2i</code>	$\text{mlc2i} \leq 3.0$	a reasonable goodness-of-fit around the peak
1	<code>mlc2o</code>	$\text{mlc2o} \leq 3.0$	a reasonable goodness-of-fit away from the peak
1	<code>mlc2il</code>	$\text{mlc2il} \leq 3.0$	a reasonable goodness-of-fit on the left side of the peak
1	<code>mlc2ir</code>	$\text{mlc2ir} \leq 3.0$	a reasonable goodness-of-fit on the right side of the peak
1	<code>mlc2ol</code>	$\text{mlc2ol} \leq 3.0$	a reasonable goodness-of-fit on the left side, away from the peak
1	<code>mlc2or</code>	$\text{mlc2or} \leq 3.0$	a reasonable goodness-of-fit on the right side, away from the peak
1	<code>asym</code>	$\text{asym} < 0.17$	a light curve symmetric around the peak
1	<code>scorr</code>	$\text{scorr}/\sqrt{\text{dof}} \leq 3.0$	no significant correlation with the seeing
1	<code>scorrs</code>	$\max \left[\text{scorrs}/\sqrt{\text{dof}} \right] \leq 3.0$	no significant correlation with the seeing on a certain timescale
1	<code>ntscale</code>	$t_{\text{FWHM}}/t_{\text{obs}} \leq 1$	the light-curve timescale detectable within the observing window
1	<code>amax</code>	$\max A \geq 1.34$	a significant peak magnification
1	<code>mlsig</code>	$\text{mlsig} \geq 5$	a significant detection of the light curve integrated over the observing window
2	<code>mlvs</code>	visual inspection	remove impostors due to moving objects or imperfect image subtraction
3	<code>mlnrpt</code>	no repeatability	no repeated variation at the candidate position on other observing nights

TABLE V. Parameters and prior ranges of point-lens finite-source (PLFS) microlensing light-curve model, used to fit each candidate's light curve (see text for the details); f_0 is a parameter to model the intrinsic flux of a source star; u_0 is the impact parameter at closest approach of the lens to the source on the sky; t_0 is the time of peak magnification; t_E is the Einstein microlensing timescale; ρ is the source radius in units of the Einstein radius. t_0^{bump} denotes the estimated time of each candidate's light-curve peak, and $\sigma(t_0^{\text{bump}})$ is the 1σ uncertainty. The lower bound of the t_E prior is set to 2 minutes, which is the shortest timescale in our cadence. The upper bound is set to t_{obs} , the duration of the observing window for each night.

Parameter	Prior
f_0	flat $[-0.5, 0.5]$
u_0	flat $[0.0, 1.5]$
t_0	flat $[t_0^{\text{bump}} - \sigma(t_0^{\text{bump}}), t_0^{\text{bump}} + \sigma(t_0^{\text{bump}})]$
t_E	flat $[2\text{min}, t_{\text{obs}}]$
ρ	flat $[0.0, 1.5]$

$\Delta t = 2$ minutes is the minimum time resolution, i.e. the cadence of our observations.

The second step is to fit the microlensing light-curve model to the measured light curve. With a model of the magnification of the microlensing $A(u)$, we model the difference flux as

$$\Delta F_i^{\text{model}} = F_0 \Delta A(u_i) \equiv F_0 \left[A(u_i) - \frac{1}{10} \sum_{i' \in \text{ref}} A(u_{i'}) \right] \quad (3)$$

where

$$u_i = \sqrt{u_0^2 + \left(\frac{t_i - t_0}{t_E} \right)^2}. \quad (4)$$

Here, we define the intrinsic flux F_0 , the peak time t_0 (the closest approach time), the impact parameter u_0 , and the Einstein time t_E . The second term in Eq. (3) corresponds

TABLE VI. The number of the microlensing candidates that passed each of the selection criteria listed in Table IV.

ID	master	bump	mlc2	mlc2i	mlc2o	mlc2il	mlc2ir	mlc2ol	mlc2or	asym	scorr	scorrs	ntscale	amax	mlsig	mlvs	mlnrpt
2014-11-24	7281	5139	1135	938	911	878	819	814	783	391	72	70	57	53	38	25	5
2017-09-20	6199	4554	1060	962	907	877	837	821	800	287	142	59	50	44	18	18	7
2020-10-21	3636	3348	361	218	206	205	196	196	195	13	5	5	3	3	0	0	0
2020-10-22	1582	1561	66	52	47	44	41	40	38	18	1	1	1	1	0	0	0
2020-11-11	348	274	16	16	15	12	11	11	11	2	0	0	0	0	0	0	0
2020-11-12	2029	1581	202	185	185	180	154	154	154	23	18	18	0	0	0	0	0
2020-11-14	2446	1959	359	343	326	312	278	270	261	38	23	22	18	17	8	7	0
2020-11-20	1714	1241	260	223	215	205	165	164	164	15	4	4	1	1	0	0	0

TABLE VII. Summary of the 12 microlensing candidates obtained after applying the selection criteria to the master catalog. Each candidate is identified by the combination of the master catalog, patch id, and objid. The second group of columns summarizes the RA, DEC position of the candidates. The third group of columns summarizes some of the summary statistics used for the candidate selection, with the degrees of freedom that are used to compute these summary statistics. The last column group summarizes the best-fit parameters of the PLFS microlensing model. Note that the parameter degeneracies are generally strong, and the parameter values shown here represent a nominal set of the parameters obtained from the Monte-Carlo chains of the light-curve fitting. The secure candidates are marked by †, and are defined as those that further satisfy `mlsig/dof` > 10.

ID	Coord.		Selection						ML params					
	master/patch/objid	RA	Dec	mlc2	asym	scorr	max A	mlsig	dof	f_0	u_0	t_0	t_E	ρ
† 2014-11-24/1,5/75	00 ^h 46 ^m 38.41 ^s	+41° 16' 43.2"	232.68	0.08	0.07	2.88	2486.89	189	-0.43	0.21	16613.35	5598.13	0.73	
† 2014-11-24/4,2/63	00 ^h 42 ^m 53.02 ^s	+40° 48' 07.6"	251.56	0.08	-0.03	1.90	3085.37	189	-0.50	0.85	16430.47	8654.20	0.93	
2014-11-24/6,7/168	00 ^h 41 ^m 20.91 ^s	+41° 41' 16.1"	120.54	0.15	-0.06	6.10	1453.65	189	-0.33	0.05	16172.20	10218.13	0.33	
2014-11-24/6,7/169	00 ^h 41 ^m 07.94 ^s	+41° 48' 54.0"	147.72	0.12	-0.06	2.21	1281.99	189	-0.27	0.68	15587.25	5763.05	0.83	
2014-11-24/7,6/96	00 ^h 40 ^m 07.90 ^s	+41° 36' 17.8"	120.79	0.13	0.14	2.56	1335.64	189	-0.32	0.48	16223.85	5374.24	0.77	
2017-09-20/1,4/46	00 ^h 46 ^m 21.70 ^s	+41° 09' 17.1"	255.28	0.14	0.10	1.52	1092.90	214	-0.45	0.87	16060.40	3632.56	0.52	
2017-09-20/3,4/31	00 ^h 44 ^m 07.74 ^s	+41° 05' 17.6"	107.61	0.05	-0.00	3.75	1488.64	214	-0.50	0.31	14589.27	16286.60	0.25	
2017-09-20/4,2/9	00 ^h 42 ^m 56.85 ^s	+40° 49' 09.8"	334.17	0.07	-0.13	2.75	1461.36	214	-0.50	0.46	4088.65	4814.50	0.42	
† 2017-09-20/5,7/45	00 ^h 42 ^m 09.81 ^s	+41° 44' 38.3"	213.67	0.07	-0.08	2.06	2210.57	213	-0.41	0.74	14173.11	7451.41	0.92	
2017-09-20/7,4/36	00 ^h 39 ^m 47.83 ^s	+41° 11' 05.0"	140.92	0.12	-0.09	3.00	1121.77	214	-0.45	0.47	14942.25	10821.83	0.57	
2017-09-20/7,6/26	00 ^h 40 ^m 13.54 ^s	+41° 31' 29.5"	184.09	0.10	-0.07	3.44	1728.40	214	-0.43	0.39	15833.30	12398.83	0.40	
† 2017-09-20/8,2/119	00 ^h 39 ^m 33.27 ^s	+40° 50' 06.6"	107.61	0.15	-0.14	2.10	2467.61	125	-0.22	0.74	15436.09	9623.68	0.78	

to the flux of the reference image that was constructed by co-adding the images of 10 best-seeing epochs [36].

For the model of the microlensing magnification $A(u)$, we use the point-lens finite-source (PLFS) model:

$$A_{\text{PLFS}}(u; \rho) = \int d\mathbf{r} s(\mathbf{r}; \rho) A_{\text{PLPS}}(\mathbf{u} + \mathbf{r}) \quad (5)$$

where $A_{\text{PLPS}}(u) = (u^2 + 2)/u/\sqrt{u^2 + 4}$ is the point-lens point-source magnification, also known as Paczyński light curve [1]. To account for the finite source size effect [28], we assume a circular disk profile with uniform brightness, given by $s(u; \rho) = \Theta(u - \rho)/2\pi\rho^2$, where Θ is the step function. The finite-source parameter ρ is the angular size of the source star normalized by the angular Einstein radius, $\rho = \theta_s/\theta_E = (R_s/d_s)/(R_E/d_E)$. We use the public code `fastlens` [37] developed in [38] to perform the integral in Eq. (5). Around each time step t_i , we average the difference flux model over an interval of $\pm\Delta t/2$ to account for the finite exposure time. For the search of best-fit parameters, we use a nested sampling rather than a minimizer to avoid getting trapped into local minima of the parameter space. As the sampling process proceeds,

we increase the temperature of the likelihood to speed up the inference.

Eqs. (3)–(5) define the model of the microlensing light-curve, which is characterized by five model parameters $\boldsymbol{\theta} = \{F_0, u_0, t_0, t_E, \rho\}$. We estimate the best-fit parameters by minimizing the chi-square

$$\chi^2(\boldsymbol{\theta}) = \sum_i \left(\frac{\Delta F_i - \Delta F_i^{\text{model}}}{\sigma(\Delta F_i)} \right)^2. \quad (6)$$

For efficient parameter inference, we use priors on model parameters, as summarized in Table V. In the PLFS model, the light curve has a single maximum, so we can infer the intrinsic flux by comparing the maximum difference flux $\max(\Delta F)$ with the maximum of the difference magnification $\max(\Delta A)$. To ensure sufficient flexibility, we allow the intrinsic flux parameter to vary by up to 50% from the estimated value: to be precise, we introduce the fractional parameter $f_0 \in [-0.5, 0.5]$ to define $F_0 = \max(\Delta F_i)/\max(\Delta A)(1 + f_0)$ [25], and use f_0 as a free parameter instead of F_0 . To summarize, our model has five parameters $\boldsymbol{\theta} = \{f_0, u_0, t_0, t_E, \rho\}$.

Using the best-fit parameters of the PLFS model obtained from the light-curve fitting, we compute the derived statistics for selection of microlensing candidates. The first one is the full-width half-maximum (FWHM) time of the magnification:

$$A(t_0 + t_{\text{FWHM}}) = 1 + \frac{\max A - 1}{2}. \quad (7)$$

In PLFS model, the FWHM time is a function of $\{u_0, t_E, \rho\}$. We apply a selection criterion on the FWHM timescale, $t_{\text{FWHM}}/t_{\text{obs}} \leq 1$ to exclude events with timescales longer than the observation duration. We define the global goodness-of-fit by the chi-square in Eq. (6) at the best fit model, denoted as `m1c2`. We also define the chi-square values, `m1c2i` and `m1c2o`, using only the data points in “in” and “out” time regime, defined by $|t_i - t_0| < t_{\text{FWHM}}$ and $|t_i - t_0| > t_{\text{FWHM}}$, respectively. Similarly, we define `m1c2i1`, `m1c2ir`, `m1c2o1`, and `m1c2o1`, which use the data points on the left or right side of the peak accordingly in “in” and “out” time domain. We apply the selection criteria that all of these chi-squared values are smaller than 3.0.

A real microlensing light curve should be symmetric with respect to its peak time [39]. We quantify the degree of asymmetry in the measured light curve by

$$\text{asym} = \frac{\sum_{i \in \text{pairs}} w_i |\Delta F_{i+} - \Delta F_{i-}|}{\sum_{i \in \text{pairs}} w_i (\Delta F_{i+} + \Delta F_{i-} - 2 \min \Delta F)}. \quad (8)$$

Here, each pair of time indices $(i+, i-)$ is chosen symmetrically around the peak time t_0 ; the summation includes only the pairs that satisfy $|t_{i\pm} - t_0| \leq t_{\text{FWHM}}$. We apply a selection criterion, requiring $\text{asym} \leq 0.17$, to exclude light curves with significant asymmetry, as such events are unlikely to be due to microlensing.

We next consider a selection to remove light curves affected by weather conditions. To quantify the impact of weather conditions, we compute the Pearson’s correlation coefficient between the light curve and the seeing, using the latter as a proxy of the weather conditions:

$$\text{scorr} = \frac{\sum_i w_i (\Delta F_i - \bar{\Delta F})(S_i - \bar{S})}{\sqrt{\sum_i w_i (\Delta F_i - \bar{\Delta F})^2} \sqrt{\sum_i w_i (S_i - \bar{S})^2}} \quad (9)$$

where S_i is the seeing at the i -th image and we use the joint inverse variance weight $w_i = 1/[\sigma(\Delta F)^2 \times \sigma(s)^2]$. The sum runs over the images within FWHM time interval centered on the peak. We apply a selection criterion that requires $\text{scorr} \leq 3.0/\sqrt{\text{dof}}$, where dof is the number of degrees of freedom used to evaluate `scorr`.

The above definition of the correlation captures the correlation between the light curve and the seeing over all time scales. However, a light curve may also exhibit correlations on shorter timescales. To account for such correlations, we introduce a timescale dependent seeing correlation, which uses the same definition as Eq. (9) but is computed using only the data points within a specific time interval corresponding to a fixed

time range $t_{i_{\text{max}}} - t_{i_{\text{min}}}$. Then we average over all possible choices of i_{max} to define the seeing correlation for a fixed timescale, `scorrs`, together with its associated mean degree-of-freedom. Our selection criteria is that all time-dependent seeing correlations must be smaller than 3σ ; that is, $\max [\text{scorrs}/\sqrt{\text{dof}}] \leq 3.0$.

For secure event selection, we also require the microlensing event to be significant. The first selection criterion is that the maximum magnification, $\max A$, predicted by the best-fit microlensing model parameters must exceed 1.34. We call this selection as `amax`. However, this criterion relies on the parameters derived from the best-fit model and does not account for the uncertainties in the light curve. To incorporate the uncertainties, we adopt the following criteria for the significance:

$$\text{mlsig} = \sum_i \left(\frac{\Delta F_i - \min[\Delta F_i^{\text{model}}]}{\sigma(\Delta F_i)} \right)^2, \quad (10)$$

where ΔF_i is the light curve data at the i -th epoch, $\min[\Delta F_i^{\text{model}}]$ is the minimum flux for the best-fit microlensing model over the interval of observational time, and $\sigma(\Delta F_i)$ denotes the observational error at the i -th epoch. We select the events requiring $\text{mlsig}/\text{dof} > 5$. This criterion can be interpreted that the data points have $\sqrt{5}\sigma = 2.23\sigma$ deviation from no-variation on average. The reason we use the minimum flux from the best-fit model is that the observed light curve is sometimes too noisy to robustly estimate the minimum flux.

Table VI summarizes the results of event selection at each selection stage. After all of these first-level selection steps, we retained 38, 18, and 8 events from 2014-11-24, 2017-09-20, and 2020-11-24 datasets, respectively. For these remaining events, we performed a visual inspection as the second-level selection. In this selection, we looked into the raw and difference images around the detected position, to assess whether the event is consistent with microlensing or instead an impostor, e.g. due to a moving object or imperfect image subtraction. We denote this visual selection as “`mlvs`” in the Table IV. We identified several impostors, and were left with 25, 18, and 7 candidate events in the 2014-11-24, 2017-09-20, and 2020-11-24 datasets, respectively.

The microlensing event rate per star is very small, so it is highly unlikely that the same star would undergo multiple microlensing events. Therefore, repeated variations for the same star (or, more precisely, at the same position) observed on different dates are very likely due to an intrinsic variable star. To ensure that the events are not due to repeating variables, we performed the forced photometry at the position of selected events on different observation dates. We examined both the light curves and the images, and removed the events showing suspicious variations in the light curve across different dates. However, note that we did not remove the events if the apparent variation on a different observation date is attributable to poor image subtraction. This selection is labeled as “`mlnrpt`” in Table IV. After this final selection,

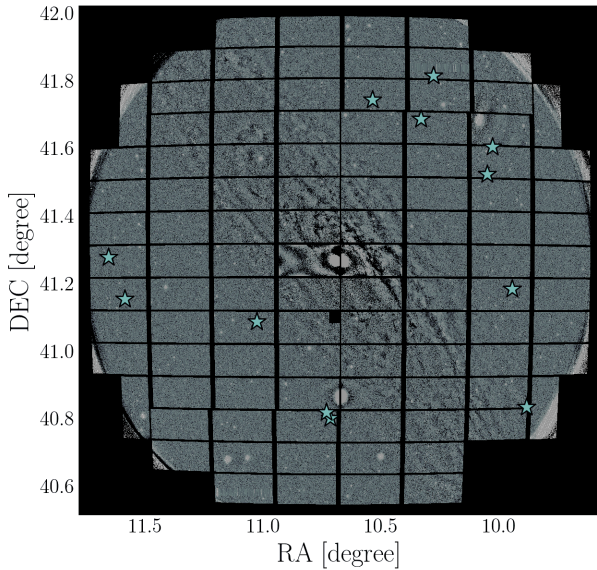


FIG. 2. An example of the image for the M31 region, where the reference image obtained under the best seeing conditions during a given night is subtracted from a target image. Most stars in the spiral disk regions of M31 are well subtracted. Point sources remaining in the difference image are candidates of variable stars. Cyan star symbols denote the locations of the 12 microlensing candidates that passed all the selection criteria.

we were left with 5 and 7 candidate events in 2014-11-24, and 2017-09-20 datasets, respectively. These 12 events constitute the sample of microlensing candidates used in the following results.

D. Candidate and secure catalogs

Table VII summarizes the properties of the selected events, which we refer to the *candidate* catalog. Appendix C also shows the light curves of these events. For each candidate event, we run an additional parameter inference using MultiNest [40] to obtain an accurate posterior distribution. In Appendix D, we show the posterior distribution of the PLFS model parameters for each candidate. Note that the degeneracies among the model parameters are generally strong, and the parameter values shown in Table VII are just a nominal set of parameters.

We notice that the light curves of some candidates have peaks at similar times during the observing night. In the simulation, we checked that the events around these times are more likely to be detected. This can be understood as follows. Since the seeing tends to be worse near the start or the end of the observation on each night, as shown in Fig. 1, a light curve whose peak occurs at those times exhibits an apparently higher correlation with seeing. Such events are therefore removed by the selection criteria based on the correlations with seeing.

In Fig. 2, we show the locations of the 12 microlensing

TABLE VIII. Ranges of parameters used to simulate microlensing light curves for estimating the detection efficiency. All parameters are randomly sampled from the listed intervals to simulate each light curve.

Parameter	Prior
u_0	flat[0.0, 2.0]
t_0	flat[0.0, t_{obs}]
$\log_{10}(t_E/t_{\text{obs}})$	flat[$\log_{10}(2 \min/t_{\text{obs}}/10.0)$, $\log_{10}(2.0)$]
ρ	flat[0.0, 2.0]

TABLE IX. Number of source stars, $N_{s,m}$, per magnitude bin m estimated in Niikura *et al.* [25].

Magnitude	$N_{s,m}$
22	675,465
23	2,326,642
24	11,827,524
25	36,627,840
26	31,793,192

candidates overlaid on an HSC image of the M31 region.

We also define the *secure* catalog by further requiring $\text{mlsig/dof} > 10$, for which we intend to select the event at higher significance although the criterion is heuristic. The events in the secure catalog are marked by \dagger in Table VII.

IV. EFFICIENCY CHARACTERIZATION

To compare the observed number of microlensing events with theoretical expectations, it is necessary to characterize the detection efficiency of microlensing events in the observed data. The efficiency is defined as the fraction of underlying microlensing events that are detected by our analysis pipeline. The efficiency depends on both the properties of individual microlensing events and the observational conditions.

We use simulations to estimate the detection efficiency. In this paper, we simulate microlensing events at the light-curve level rather than at the image level. This method was validated by Niikura *et al.* [25], which demonstrated that the efficiencies estimated from light-curve-level simulations are consistent with those obtained from image-level simulations. For every combination of observation date/time and HSC patch, we simulate 10,000 light curves for PLFS microlensing events:

$$\Delta F(t_i) = F(t_i) - \frac{1}{10} \sum_{j \in \text{ref}} F(t_j) + N_i, \quad (11)$$

with

$$F(t_i) = F_0 A(t_i; \boldsymbol{\theta}). \quad (12)$$

Here $\boldsymbol{\theta} = (u_0, t_0, t_E, \rho)$ is the set of microlensing model parameters, each drawn uniformly from

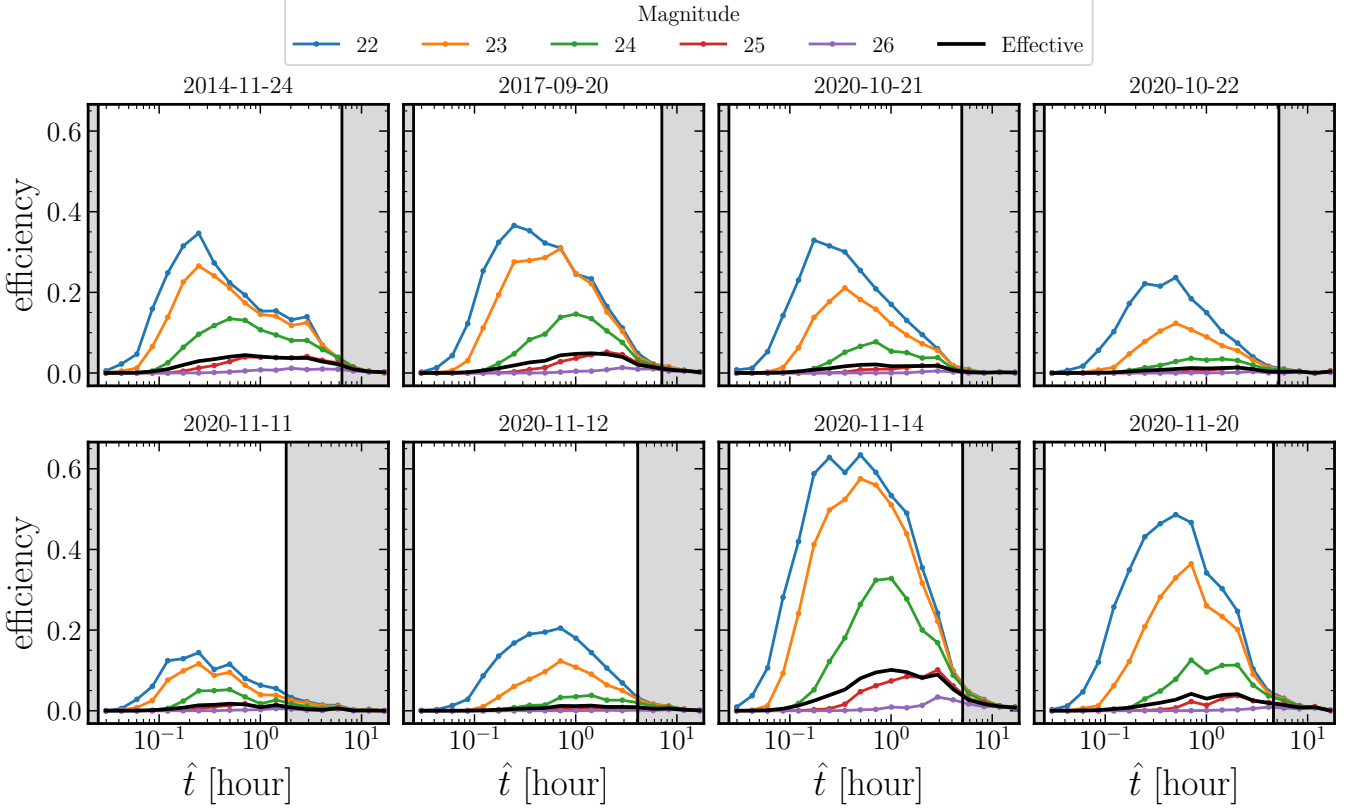


FIG. 3. The detection efficiency of the microlensing events as a function of the microlensing light-curve timescale $\hat{t} \equiv t_E \sqrt{u_T^2(\rho) - u_0^2}$. Each panel shows the detection efficiency for each observation data, as indicated in the title of panel. Different colors show the efficiency for source stars with different intrinsic brightness, i.e., (22, 23, 24, 25, 26) mag, respectively. For each combination of observation date, source brightness, and HSC patch, we simulated 10,000 realizations of microlensing light curves by randomly drawing model parameters from the priors listed in Table VIII and adding Gaussian random noise whose amplitude is estimated from the corresponding data in each HSC patch and on each observation date. The black curve in each panel indicates the *effective* efficiency, obtained by integrating the brightness-dependent efficiencies weighted by the brightness distribution of source stars in M31, as defined in Eq. (13). The shaded regions in each panel indicate the regions of microlensing timescales that are difficult to detect in each dataset: for each observation data, the upper timescale cut corresponds to T_{eff} listed in Table I.

the prior range in Table VIII. For the intrinsic flux F_0 , we adopt discrete values in photon counts: $\{10^{0.4 \times 5}, 10^{0.4 \times 4}, 10^{0.4 \times 3}, 10^{0.4 \times 2}, 10^{0.4 \times 1}\}$ corresponding to $\{22, 23, 24, 25, 26\}$ mag, respectively. The second term N_i in Eq. (11) is the noise term, which is drawn from a normal distribution with zero mean and a standard deviation estimated by averaging the errors of all light curves in the corresponding master catalog in the patch under consideration. After running simulations in each magnitude bin m , we estimate the efficiency $\epsilon_m^n(\hat{t})$ as the ratio of the number of detected events to the number of injected events for each microlensing timescale $\hat{t} \equiv t_E \sqrt{u_T^2(\rho) - u_0^2}$ for each night n . After running the entire process described above, we found that the efficiency is low and noisy in some magnitude bins; therefore, we performed an additional set of simulations with four times as many realizations.

We also define the effective efficiency by averaging the efficiencies in different magnitude bins, weighted by the

number of background source stars:

$$\epsilon_{\text{eff}}^n(\hat{t}) = \frac{1}{N_{s,\text{tot}}} \sum_m \epsilon_m^n(\hat{t}) N_{s,m}, \quad (13)$$

where $N_{s,m}$ is the number of source stars in the magnitude bin m , and $N_{s,\text{tot}}$ is the sum of them. We use the numbers of source stars in each magnitude bin, estimated in Ref. [25], as summarized in Table IX.

Fig. 3 shows the estimated detection efficiency as a function of the microlensing light curve timescale, \hat{t} . We first note that the efficiency clearly depends on the observation date, reflecting varying observing conditions. In particular, the efficiencies for 2014-11-24, 2017-09-20, and 2020-11-14 are higher than the other dates, consistent with expectations from the typical seeing on those nights, as summarized in Table I. However, we suspect that the efficiency for 2020-11-14 night would be overestimated, because we did not detect any microlensing candidates on that night. We think that this is due to the rel-

atively poor seeing conditions compared to those on the nights of 2014-11-24 and 2017-09-20, during which the microlensing candidates were detected, as can be found from Fig. 1. In Appendix A, we checked that the efficiency of microlensing candidate detection is sensitive to the seeing conditions of the reference image used in the image difference technique. Therefore, the relatively poor seeing on 2020-11-14 limits the sensitivity of microlensing detection. However, the light curve simulations do not adequately reproduce the degraded uncertainties. This is beyond the scope of this paper, and we will revisit it in the future. In this paper, we include the microlensing detection efficiency for 2020-11-14 in the following results.

We also note a non-zero efficiency even for light curve timescales longer than the observational duration of each night (~ 7 hours). This is because partial light-curve coverage can still be fit within the statistical errors by different combinations of the parameters, owing to parameter degeneracies. Consequently, some of such simulated light curves can pass the selection criteria and be detected.

V. LIKELIHOOD MODELING FOR POPULATION PARAMETER INFERENCE

As described in Section III, we retain 5 and 7 microlensing candidate events from the 2014-11-24 and 2017-09-20 data, while no events are selected from the other observing dates. Additionally, we obtained the posterior distribution of the microlensing parameters for each of these candidate microlensing events. In this section, we describe how we constrain the parameters of the PBH population model, λ , from these observed data.

The simplest way is to construct the Poisson likelihood for the observed number of the events and compare it with the theoretical prediction based on the mass function under consideration:

$$\mathcal{L}_{\text{Po}}(\{N_{\text{obs},n}\}|\lambda) = \prod_{n=1}^8 P_{\text{Po}}(N_{\text{obs},n}|N_{\text{exp},n}(\lambda)) \quad (14)$$

where $P_{\text{Po}}(N_{\text{obs}}|N_{\text{exp}})$ is the Poisson probability of observing N_{obs} events given an expectation of N_{exp} events, and $N_{\text{obs},n}$ and $N_{\text{exp},n}$ are the observed and expected numbers of events for each night indexed by n . The expected number of events depends on the PBH population parameters λ . In the next section, we will consider several working hypotheses to infer the PBH population parameters. Since we consider different values of N_{obs} , depending on the level of confidence in the candidates, we do not specify the value of $N_{\text{obs},n}$ in this section. Because the Poisson probability only tests the number of the observed events, it is only sensitive to the abundance parameter, and cannot be used to infer other population parameters such as mass scale.

To constrain PBH population parameters beyond the abundance parameter, we employ hierarchical Bayesian

inference that incorporates the light curve information for each microlensing candidate, in addition to the number of microlensing events for each night. If the microlensing light curve has a sufficient signal-to-noise ratio, the PLFS parameters can be estimated precisely, which in turn can be used to infer the lens mass, i.e., the PBH mass [41]. However, the different candidates have different precisions in the estimation of the PLFS parameters, as shown in Appendix D. We employ the method in Ref. [42] to combine the light curve information from the different candidates [see also 43, for earlier work on this problem].

For notational simplicity, we denote the j -th light curve data in the n -th night by the vector $\mathbf{d}_j^n = \{\Delta F_i\}$ in the following. The total likelihood for a set of the light curve data $\{\mathbf{d}_j^n\}$ can be modeled, following Eq. (7) of Ref. [42], as

$$\mathcal{L}_{\text{LC}}(\{\mathbf{d}_j^n\}|\lambda) = \prod_{n=1}^8 \prod_{j=1}^{N_{\text{obs},n}} \mathcal{L}_{\text{LC}}(\mathbf{d}_j^n|\lambda) \quad (15)$$

with

$$\mathcal{L}_{\text{LC}}(\mathbf{d}_j^n|\lambda) = \frac{\int dd \int d\theta P(\mathbf{d}_j^n|\theta) P_{\text{pop}}(\theta, d|\lambda)}{\int dd \int d\theta \epsilon_{\text{eff}}^n(\theta) P_{\text{pop}}(\theta, d|\lambda)}, \quad (16)$$

where $P(\mathbf{d}_j^n|\theta)$ is the likelihood of observing the light curve \mathbf{d}_j^n for a given set of PLFS parameters θ on the n -th night, and $\epsilon_{\text{eff}}^n(\theta)$ is the detection efficiency for that night, given as a function of θ . We note that the population model, specified by λ , also provides the probability distribution for PBHs at the distance d , but the light curve itself is not sensitive to d because of parameter degeneracies. Therefore, we assume the likelihood of observing the light curve depends only on θ , not on d . We also note that the PLFS parameters t_0 and f_0 do not contain any information about the population, and thus we implicitly marginalize over these variables and assume $\theta = \{t_E, u_0, \rho\}$. The population distribution $P_{\text{pop}}(\theta|\lambda)$ describes the distribution of events for a given set of the population parameters λ , and is defined by the normalized differential event rate:

$$\frac{d\Gamma}{dd\theta}(\lambda) = N(\lambda) P_{\text{pop}}(\theta, d|\lambda) \quad (17)$$

with $\int d\theta P_{\text{pop}}(\theta|\lambda) = 1$. See Appendix B for the detailed definition of the differential event rate.

By multiplying $N(\lambda)$ to both the numerator and denominator of Eq. (16), we can replace the population probability by the differential event rate:

$$\mathcal{L}_{\text{LC}}(\mathbf{d}_j^n|\lambda) = \frac{\int dd \int d\theta P(\mathbf{d}_j^n|\theta) \frac{d\Gamma}{dd\theta}(\lambda)}{\int dd \int d\theta \epsilon_{\text{eff}}^n(\theta) \frac{d\Gamma}{dd\theta}(\lambda)}. \quad (18)$$

Then the integral in the denominator yields the standard event rate as a function of the population parameters. In the previous section, we checked that the efficiency mainly depends on the PLFS parameters through \hat{t} , and

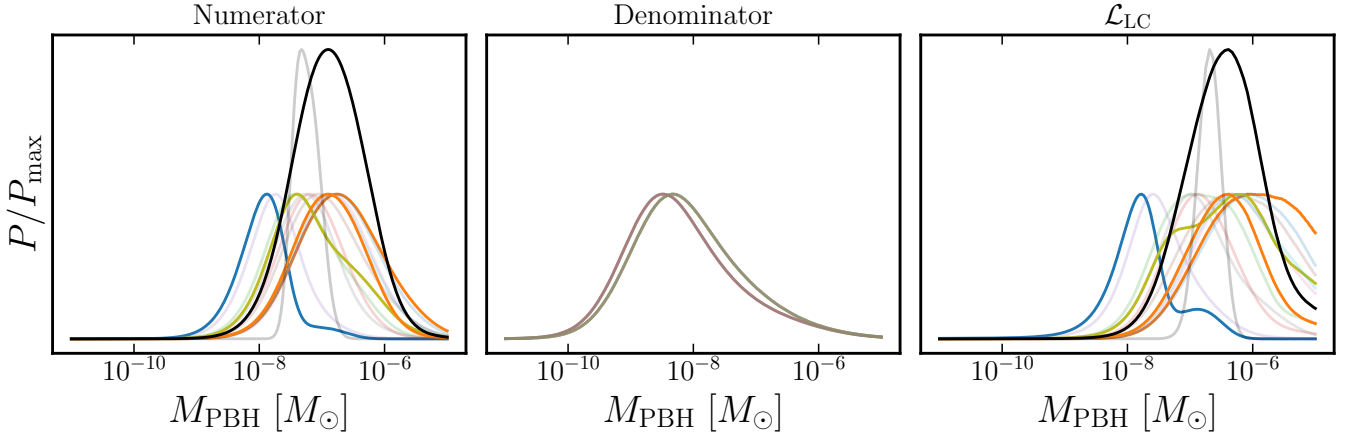


FIG. 4. The rightmost panel shows the profiles of the light-curve likelihoods for each of the 12 microlensing candidates, computed using Eq. (18). Here we adopt the monochromatic PBH mass function defined in Eq. (23). The colored lines are the likelihoods for individual candidates $\mathcal{L}_{\text{LC}}(\mathbf{d}_j^n | M_{\text{PBH}})$, each normalized by their maximum values. The bold lines show the likelihoods for the 4 secure candidates (see Table VII). The joint likelihood $\mathcal{L}_{\text{LC}}(\{\mathbf{d}_j^n\} | M_{\text{PBH}})$ for all the candidates or for the 4 secure candidates is shown by the thin gray or bold black line, respectively, and each profile is normalized such that its peak is twice as high as those of the individual likelihoods. The left and middle panels show the numerator and denominator of the light-curve likelihoods. Note that, since the candidates are obtained only on 2014-11-24 and 2017-09-20, the middle panel contains only two lines.

therefore the denominator of Eq. (18) can be simplified as

$$\Gamma_n(\boldsymbol{\lambda}) = \int dd \int d\hat{t} \epsilon_{\text{eff}}^n(\hat{t}) \frac{d\Gamma}{d\hat{t}}(\boldsymbol{\lambda}). \quad (19)$$

The detailed form is given by Eq. (B4).

In Section III D and Appendix D, we show that the PLFS parameters $\boldsymbol{\theta}$ have strong degeneracies among themselves in their posterior distributions. This means that the multidimensional integral in the numerator of Eq. (18) is difficult to reduce to a lower-dimensional integral. By following Mandel *et al.* [42] and using appropriate changes of variables, we evaluate the integral in the numerator using the Monte-Carlo integration with the posterior samples obtained from the light curve fitting. We leave the details of the computation to Appendix E.

To simultaneously constrain the abundance and other population parameters of PBHs (e.g., their mass and mass function), we combine the Poisson likelihood in Eq. (14) with the light-curve likelihood in Eq. (18):

$$\mathcal{L}(\{\mathbf{d}_j^n\}, \{N_{\text{obs},n}\} | \boldsymbol{\lambda}) = \mathcal{L}_{\text{Po}}(\{N_{\text{obs},n}\} | \boldsymbol{\lambda}) \times \mathcal{L}_{\text{LC}}(\{\mathbf{d}_j^n\} | \boldsymbol{\lambda}). \quad (20)$$

From Bayes theorem, we obtain the posterior distribution of $\boldsymbol{\lambda}$ for given datasets

$$\mathcal{P}_{\text{Po}}(\boldsymbol{\lambda} | \{N_{\text{obs},n}\}) = \mathcal{L}_{\text{Po}}(\{N_{\text{obs},n}\} | \boldsymbol{\lambda}) \Pi(\boldsymbol{\lambda}) \quad (21)$$

or

$$\mathcal{P}(\boldsymbol{\lambda} | \{\mathbf{d}_j^n\}, \{N_{\text{obs},n}\}) = \mathcal{L}(\{\mathbf{d}_j^n\}, \{N_{\text{obs},n}\} | \boldsymbol{\lambda}) \Pi(\boldsymbol{\lambda}) \quad (22)$$

up to a normalization constant, respectively. The former (Eq. (21)) corresponds to the result obtained using

only the number of microlensing events, while the latter (Eq. (22)) corresponds to the result obtained by combining the number of events with the light-curve information for each candidate.

Fig. 4 shows the profiles of the light-curve likelihoods for the individual events, as well as their joint profile, assuming a monochromatic mass function for PBHs:

$$\frac{dn}{d \ln M} = f_{\text{PBH}} \delta^D(\ln M - \ln M_{\text{PBH}}), \quad (23)$$

where the population parameters are $\boldsymbol{\lambda} = \{f_{\text{PBH}}, M_{\text{PBH}}\}$. For the monochromatic mass function, the light-curve likelihoods do not depend on the abundance parameter f_{PBH} , and only depends on M_{PBH} ; $\mathcal{L}_{\text{LC}}(\{\mathbf{d}_j^n\} | \boldsymbol{\lambda}) = \mathcal{L}_{\text{LC}}(\{\mathbf{d}_j^n\} | M_{\text{PBH}})$. Therefore, the profiles of the light-curve likelihoods is shown as functions of M_{PBH} in the figure.

The light-curve likelihood for a more generic mass function $\frac{dn}{d \ln M}(M; \boldsymbol{\lambda})$ can be easily obtained by extending the above method. We convolve the numerator and denominator of the light-curve likelihood separately with the mass function, and then take the ratio of the convolved quantities to obtain the desired likelihood.

VI. RESULTS

In this section, we constrain the abundance of compact objects, such as PBHs, in the dark matter halos of the Milky Way and M31, using the likelihoods defined in the previous section. We consider three different working hypotheses.

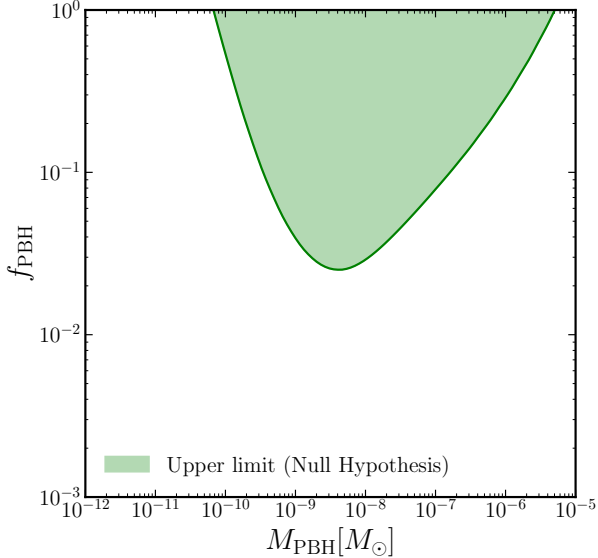


FIG. 5. The 95% C.L. exclusion region of the PBH abundance parameter f_{PBH} for each mass scale of M_{PBH} (green region). Here, f_{PBH} is the PBH mass fraction to the total dark matter in the Milky Way and M31 halo regions. We obtained the region assuming a monochromatic mass function under the null hypothesis, namely that all our candidates are false positives.

A. Null hypothesis: Upper limit on the PBH abundance

In the null hypothesis, we assume that all the candidate events are false positive caused by, e.g. variable stars, rather than by microlensing due to PBH. Under this hypothesis, we derive an upper limit on the abundance of compact objects, such as PBHs, as a component of dark matter. More specifically, we use the Poisson likelihood defined in Eq. (14) by setting $N_{\text{obs},n} = (0, 0, 0, 0, 0, 0, 0)$. In this hypothesis, we consider the monochromatic PBH mass function, defined in Eq. (23), and derive an upper bound on f_{PBH} as a function of PBH mass scale M_{PBH} by imposing $\mathcal{L} > 0.05$, which corresponds to 95% confidence level (C.L.). This means that we treat $\boldsymbol{\lambda} = \{f_{\text{PBH}}\}$ as a model parameter and constrain it at each of the varied mass scales M_{PBH} .

Figure 5 shows the upper limit. The constraint is not improved compared to Niikura *et al.* [25] or the subsequent work Smith *et al.* [44], even though we use a larger data under the same hypothesis. This is because we include the finite source size effect in our analysis pipeline, which lowers the efficiency, since the microlensing events with finite source-star size generally produce smaller magnifications.

B. PBH hypothesis: Posteriors for the PBH mass function parameters

In this section, we consider PBH hypothesis, where we assume that all the events in the *candidate* catalog are caused by PBHs, with probabilities given by the likelihood function. This hypothesis allows us to derive posterior distributions for the PBH abundance parameters, or more generally for parameters that characterize PBH mass function, using the candidate catalog summarized in Table VII. In this case, we set $N_{\text{obs},n} = (5, 7, 0, 0, 0, 0, 0, 0)$.

We start with deriving the allowed region of $\boldsymbol{\lambda} = (f_{\text{PBH}}, M_{\text{PBH}})$ for the monochromatic mass function (Eq. (23)), based on the PBH hypothesis. We first derive the parameter constraints using the likelihood for the number of microlensing events, as defined in Eq. (21). We adopt uniform priors on $\ln f_{\text{PBH}}$ and $\ln M_{\text{PBH}}$. The gray contours in Fig. 6 show the resulting constraints on $(f_{\text{PBH}}, M_{\text{PBH}})$. Because we use only the number of detected events, the mass scale is not constrained at all, and only the abundance parameter f_{PBH} is constrained at each mass scale M_{PBH} . This means that the parameters in the gray bands predict nearly identical event rates and therefore cannot be distinguished only through the observed number of events.

Next, we examine the case in which the light-curve information for each candidate is incorporated together with the number of events, as defined in Eq. (22). The blue contours in Fig. 6 show the allowed region of the PBH mass function parameters, $(f_{\text{PBH}}, M_{\text{PBH}})$. It is clear that the constraint on mass scale is significantly improved, compared to the gray contours.

Motivated by the constraining power on the PBH mass scale demonstrated above, we also consider the case in which PBHs follow the power-law mass function defined by

$$\frac{dn}{d \ln M} = f_{\text{PBH}} p \left(\frac{M}{M_{\text{min}}} \right)^p \Theta(M - M_{\text{min}}), \quad (24)$$

where $p < 0$ is the power-law index, for which we fix $p = -1$, $\Theta(x)$ is the Heaviside function, defined as $\Theta(x) = 1$ if $x > 0$ and $\Theta(x) = 0$ otherwise, and M_{min} is the minimum PBH mass scale. This model is normalized such that the total abundance becomes f_{PBH} after integrating over M_{PBH} . The model parameters are $\boldsymbol{\lambda} = (f_{\text{PBH}}, M_{\text{min}})$. We adopt uniform priors on $\ln f_{\text{PBH}}$ and $\ln M_{\text{min}}$.

The right panel of Fig. 6 shows the allowed region for these parameters. We notice that the contours look similar to those for the monochromatic mass function, but are slightly shifted toward lower masses. This is because the power-law mass function produces microlensing events from PBHs at mass scales greater than the minimum mass scale, $M > M_{\text{min}}$.

In Appendix F, we present some tests of more complicated and extended mass functions, which are motivated by the theory of PBH formation.

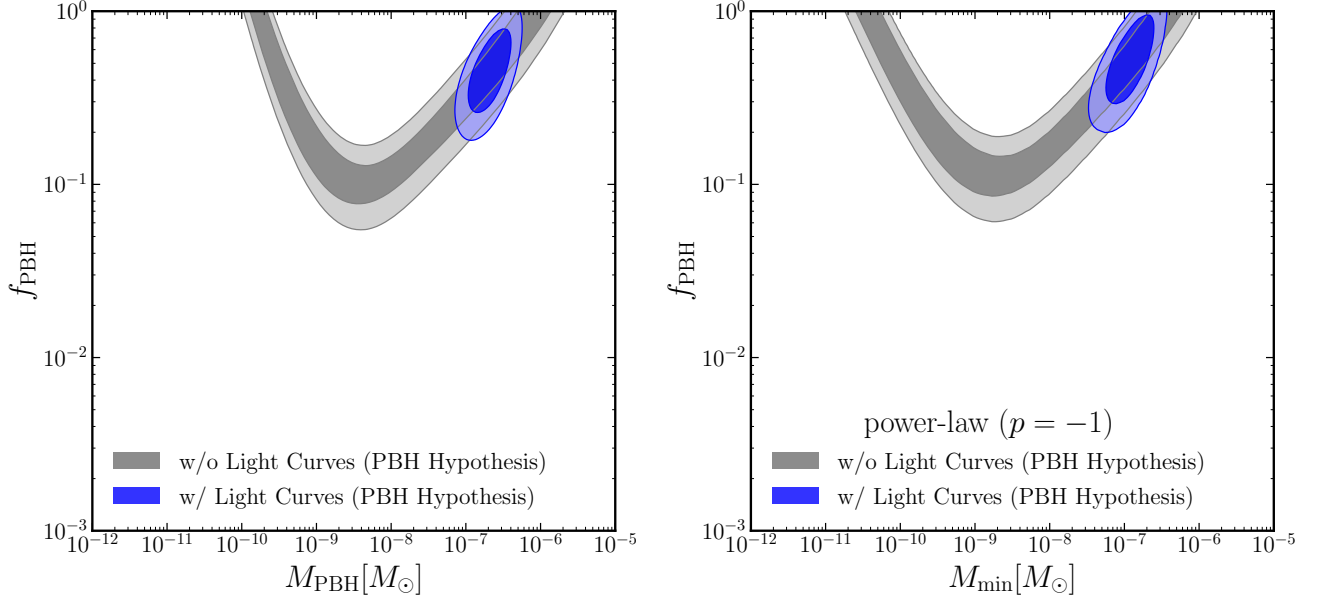


FIG. 6. The shaded regions show the 68% and 95% C.L. allowed regions of the PBH abundance parameters under the PBH hypothesis, where we assumed that all the candidates are due to PBH microlensing. *Left*: The posterior distributions obtained assuming the monochromatic PBH mass function. The gray contours are obtained using the Poisson likelihood for the number of candidates. In this case we obtain the allowed range only for f_{PBH} at each PBH mass scale. The blue contours are obtained using the likelihood that further incorporates the light-curve information for each candidate (Fig. 4) together with the Poisson likelihood. In this case, the PBH mass scale is also constrained simultaneously with f_{PBH} . *Right*: Similar results, but assuming the power-law PBH mass function defined in Eq. (24). We considered the fixed power-law index $p = -1$ for the mass function $dn_{\text{PBH}}/d \ln M_{\text{PBH}} \propto M^p$, where M_{min} is a parameter that characterizes the minimum PBH mass scale.

C. PBH hypothesis with the secure microlensing candidates

Lastly in this section, we consider a scenario that lies between the previous two hypotheses; we assume that only the secure microlensing events defined in Section III D are caused by PBHs. The result is shown in Fig. 7. Because the number of the events used in the light-curve likelihood (Eq. (18)) is smaller than the previous section, the constraint on the mass scale is weakened. Also, the uncertainty on the abundance parameter f_{PBH} is increased because of the smaller number of events used. As shown in Fig. 4, the typical mass scales indicated by the light-curve likelihoods are similar in the candidate and secure catalogs; therefore, the central mass scale does not change from that shown in Fig. 6. However, the number of the events is smaller under this hypothesis than under the previous ones, and as a consequence the data prefer a smaller f_{PBH} .

VII. DISCUSSION AND CONCLUSION

A. Interpretation of Microlensing Candidates

We compare our results obtained with the HSC data to those from other major (micro)lensing surveys and

experiments. Fig. 8 summarizes the constraints on the PBH abundance, f_{PBH} , assuming a monochromatic PBH mass function. The solid lines represent upper limits derived under the null hypothesis from various microlensing searches. The dashed lines indicate allowed regions of the PBH parameters, assuming that microlensing candidates are genuine, as well as the region indicated by 5-year OGLE data (denoted as “OGLE?”) [19, 51].

First, we compare our null-hypothesis upper limits with those obtained in Niikura *et al.* [25], which were derived using an earlier HSC dataset based on the 2014 data alone (subset of the dataset used in this work). Although both studies are based on HSC observations of M31, our analysis incorporates a significantly expanded dataset, combining the 2014, 2017, and 2020 observations, as well as a revised treatment of the detection efficiency. Despite the increased data volume, our resulting upper limits are less stringent than those reported in Niikura *et al.* [25]. This difference arises primarily from the fact that we include finite-source-size effects in the efficiency estimation. While Niikura *et al.* [25] injected only point-source microlensing events, leading to a relatively high detection efficiency, our analysis includes finite-source events in the injection process. As a consequence, the overall detection efficiency is reduced, which lowers the expected number of events and results in relaxed upper limits under the null hypothesis. This difference reflects not a loss of sensitivity in the data themselves, but rather a more realistic

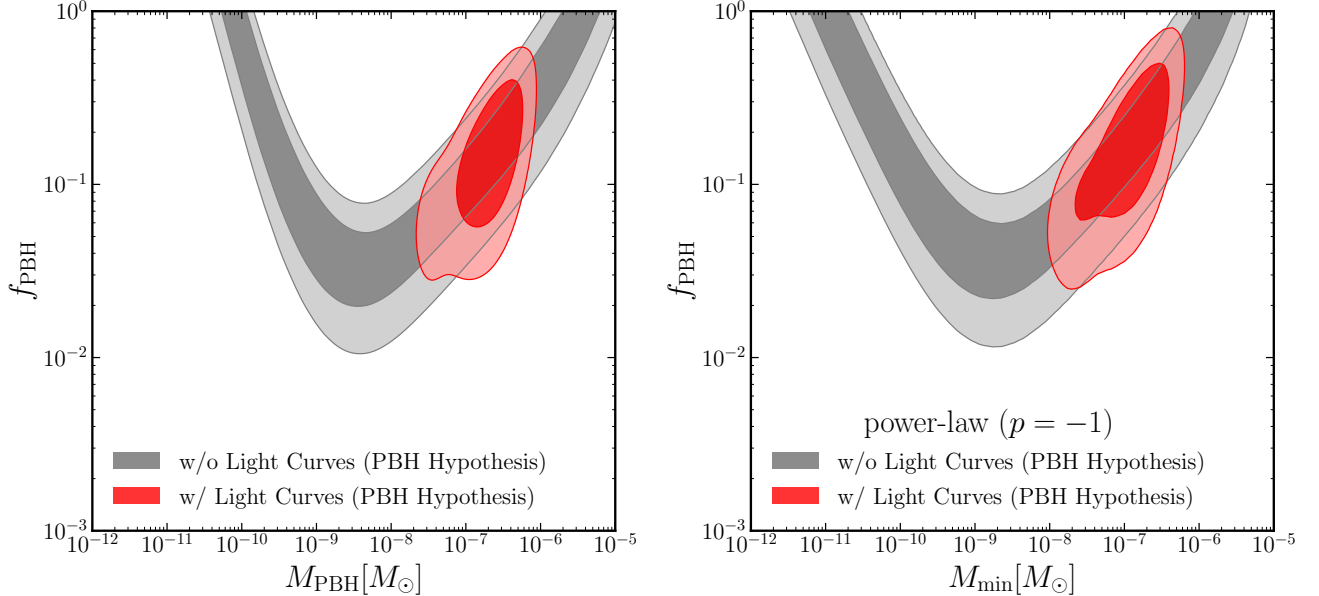


FIG. 7. Similar to Fig. 6, but showing the results obtained using only the 4 secure candidates (Table VII). A smaller abundance parameter is preferred compared to the previous figure, as fewer events are attributed to PBH in this hypothesis. The mass scale is almost the same though with larger statistical uncertainty.

treatment of microlensing signals in the presence of finite source effects.

In contrast, the allowed region of PBH parameter space derived under the PBH microlensing hypothesis is consistent with most existing constraints shown in Fig. 8, owing to differences in the mass ranges to which each experiment is most sensitive. However, it is in clear tension with the upper limits reported by the OGLE high-cadence microlensing result by Mróz *et al.* [20]. Several possible explanations for this discrepancy can be considered.

- First, it is possible that the candidate microlensing events identified in this work are false positives, in which case the PBH hypothesis would be disfavored. The HSC observations are conducted in a single photometric band, which prevents us from performing chromatic tests that could help distinguish microlensing from intrinsic stellar variability. In addition, because our analysis relies on pixel lensing, the source stars are not resolved, and their intrinsic properties cannot be directly constrained. If such information were available, source colors or absolute magnitudes could be used to infer distances and stellar types, providing a means to identify contaminating variable stars. While we cannot exclude this possibility, a detailed investigation of source properties is beyond the scope of this paper.
- Second, the detection efficiency may be underestimated. In our analysis, the efficiency is assumed to be determined by a single representative param-

eter combination, $\hat{t} = 2t_E\sqrt{u_T(\rho)^2 - u_0^2}$ which effectively compresses the full, high-dimensional parameter space into a one-dimensional description. However, it is conceivable that the efficiency depends on the full set of microlensing parameters in a non-trivial manner. In particular, there may exist regions of parameter space where the efficiency drops sharply, and events in such regions would be systematically missed. If these regions are improperly marginalized over, the resulting efficiency could be misestimated. A fully general treatment would require simulations spanning the entire high-dimensional parameter space, which is computationally prohibitive for the present study. Nevertheless, it may be possible in future work to construct an efficient emulator of the detection efficiency using machine-learning techniques, recasting the problem as a Bernoulli probability estimation task that can be trained with a limited number of simulations. Such an approach lies beyond the scope of this paper.

- Third, the OGLE high-cadence survey reports two remaining candidate events, one of which is attributed to a flare from a dwarf star, while the other is interpreted as being caused by a lens in the Milky Way disk. If either of these events were instead due to PBH microlensing, the corresponding OGLE high-cadence upper limits would be weakened. However, even under the extreme assumption that both events are PBH-induced, the resulting constraints would still be insufficient to reconcile the discrepancy with the HSC results, which differ

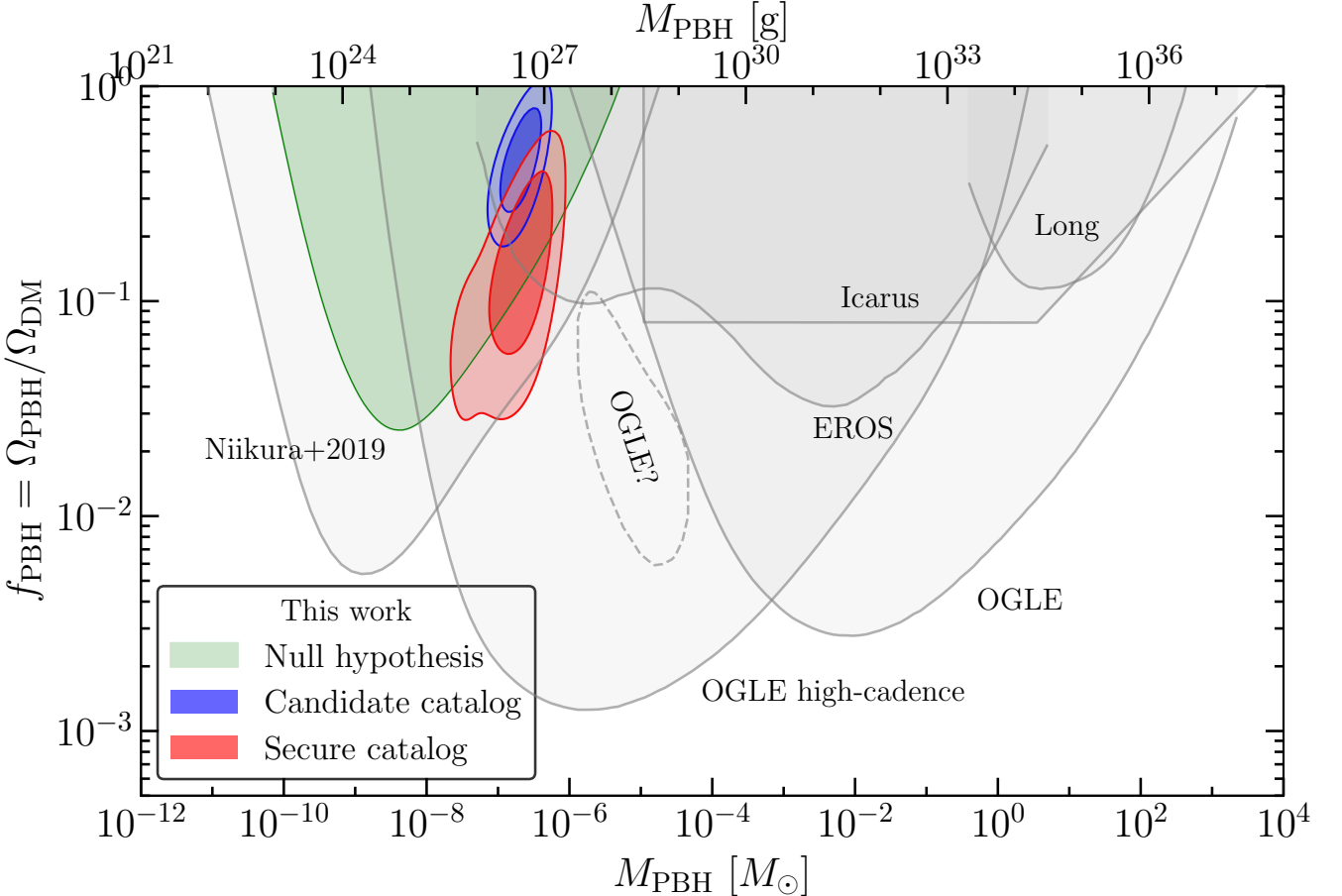


FIG. 8. Comparison of the results in this paper with other results. The solid lines show the 95% C.L. upper limits on f_{PBH} at each PBH mass scale for a monochromatic mass function, while the dashed lines show the 95% C.L. allowed regions. The upper limits from OGLE experiments denoted by “OGLE” and “OGLE high-cadence” at high and low mass scales are from Mroz *et al.* [45, 46] and Mróz *et al.* [20] respectively. The allowed region denoted by “OGLE?” is from Niikura *et al.* [19] derived using the 6 short-time scale candidate events in OGLE experiment. The upper limit denoted by “EROS” is from Tisserand *et al.* [47]. The upper limit denoted by “Icarus” is from Oguri *et al.* [48]. The upper limit denoted by “Long” is from Blaineau *et al.* [49]. We used Kavanagh [50] to plot the upper limits from other papers.

at the level of nearly two orders of magnitude.

- Fourth, it is possible that the candidate events detected in this work are all due to lenses in the Milky Way disk rather than PBHs. Because the line of sight toward M31 lies at a lower Galactic latitude than those toward the LMC or SMC, contamination from disk lenses could in principle be more significant than in the OGLE high-cadence observations. To assess this possibility, we estimated the expected number of microlensing events due to Milky Way disk lenses using a Galactic disk model in Han and Gould [52]. We find that the expected contribution is extremely small, e.g. $N_{\text{exp}}^{\text{disk}} \simeq 10^{-6}$ for 2014-11-24 night, and therefore negligible for the present analysis.

In summary, it is difficult to attribute the tension between the HSC allowed region and the OGLE high-

cadence upper limits to any single effect. The OGLE high-cadence survey reports $\mathcal{O}(10^3)$ expected events but detects no more than two candidates, implying a discrepancy with the HSC results at the level of approximately two orders of magnitude. Resolving this tension will likely require a combination of improved control of detection efficiencies, better characterization of contaminating populations, and independent datasets with complementary systematics.

B. Limitations and Future Improvements

While the present analysis demonstrates the capability of imaging data to detect short-timescale microlensing events toward M31, several limitations remain, which also point to clear directions for future improvements.

First, the current data set is based on observations in

a single photometric band (the r band). Microlensing is, in principle, an achromatic phenomenon, as the gravitational deflection of light does not depend on wavelength in the geometric optics regime. Therefore, observing consistent magnification signals in multiple bands provides a powerful discriminator between genuine microlensing events and intrinsic stellar variability. Although chromatic effects may arise in the wave-optics regime or due to finite-source effects combined with limb darkening, multi-band observations would significantly enhance the robustness of event classification. Future surveys with multi-band time-series imaging will allow us to explicitly test achromaticity and reduce contamination from variable stars.

Second, the temporal coverage of observations plays a critical role in the detectability of microlensing events. In the current strategy, observations are often limited to partial nights, which restricts the effective time baseline. Extending the coverage to full-night observations would substantially improve sensitivity, even for short-timescale events. This is because the expected number of detectable events increases more than linearly with the observation time, as longer continuous coverage improves the overall observing time as well as the detection efficiency. Therefore, having one night observing allocation would be helpful to maximize the sensitivity to the microlensing events.

Third, the false positive rate remains an important concern. Although the current selection criteria are designed to suppress known classes of contaminants, such as variable stars and subtraction artifacts, residual false positives may still be present. A more systematic characterization of the false positive rate, potentially using dedicated control samples or injection-recovery tests on real data, will be necessary to fully quantify the purity of the event sample. Such studies will also inform the optimal balance between completeness and reliability in future analyses.

Fourth, the detection efficiency is currently characterized using a limited set of representative parameters, typically focusing on a single timescale variable \hat{t} . In reality, the efficiency depends on multiple correlated parameters, including event timescale, impact parameter, finite-source size parameter. A more accurate efficiency model that accounts for this multi-dimensional parameter dependence would lead to a more precise inference of the underlying microlensing event rate and, consequently, tighter constraints on compact-object populations. Developing such a method is an important goal for future work.

Finally, image quality, particularly the seeing condition, plays a crucial role in our analysis. Since the detection relies on image subtraction, high-quality reference images with good seeing are essential for minimizing residuals and improving sensitivity to faint and short-duration events. Future observations that prioritize excellent seeing for reference image construction, as well as improved point-spread-function modeling, will further

enhance the performance of difference imaging.

In summary, while the present study establishes a solid foundation for microlensing searches toward M31, incorporating multi-band observations, longer and more continuous temporal coverage, improved false-positive control, more sophisticated efficiency modeling, and higher-quality reference imaging will be essential for fully exploiting the potential of this approach in future surveys.

Finally, future next-generation surveys provide useful prospects for short-timescale microlensing searches based on difference imaging, as adopted in this study, from different perspectives. The Nancy Grace Roman Space Telescope has a highly stable and well-characterized point-spread function as a space-based telescope, which is expected to reduce systematic errors in difference imaging analyses in crowded stellar fields. This property will allow more precise measurements of microlensing light curves, including short-timescale events and finite-source effects. On the other hand, the Vera C. Rubin Observatory (LSST) will provide wide-field, long-term time-series observations, which are expected to increase the microlensing event sample and to reduce statistical uncertainties in the event rate estimation. In addition, its high observing cadence and long temporal baseline will provide important information for evaluating the sensitivity to short-timescale events. Considering these characteristics, next-generation surveys are expected to provide useful data sets for future applications and tests of the method presented in this work.

ACKNOWLEDGMENTS

We thank Takayuki Ohgami for helping us analyzing the image data at the early stage of the paper. We thank Tsuyoshi Terai, Mirko Simunovic, and Takuya Fujiyoshi for the service as Support Astronomers. We thank Hiroko Niikura for providing the previous analysis pipeline. SS thank Satoshi Toki for a useful discussion about the hierarchical Bayesian inference of the PBH mass function, and providing us with the code to calculate the event rate by disk stars. We thank Alex Kusenko for the useful comments on the theoretical PBH model. SS thank the Center for Particle Cosmology in University of Pennsylvania, where part of this work was carried out. This work was supported in part by JSPS KAKENHI Grant Number 23KJ0747, and by World Premier International Research Center Initiative (WPI Initiative), MEXT, Japan.

The Hyper Suprime-Cam (HSC) collaboration includes the astronomical communities of Japan and Taiwan, and Princeton University. The HSC instrumentation and software were developed by the National Astronomical Observatory of Japan (NAOJ), the Kavli Institute for the Physics and Mathematics of the Universe (Kavli IPMU), the University of Tokyo, the High Energy Accelerator Research Organization (KEK), the Academia Sinica Institute for Astronomy and Astrophysics in Taiwan (ASIAA), and Princeton University. Funding was con-

tributed by the FIRST program from the Japanese Cabinet Office, the Ministry of Education, Culture, Sports, Science and Technology (MEXT), the Japan Society for the Promotion of Science (JSPS), Japan Science and Technology Agency (JST), the Toray Science Foundation, NAOJ, Kavli IPMU, KEK, ASIAA, and Princeton University.

This paper makes use of software developed for Vera C. Rubin Observatory. We thank the Rubin Observatory for making their code available as free software at <http://pipelines.lsst.io/>.

This paper is based on data collected at the Subaru Telescope and retrieved from the HSC data archive system, which is operated by the Subaru Telescope and Astronomy Data Center (ADC) at NAOJ. Data analysis was in part carried out with the cooperation of Center for Computational Astrophysics (CfCA), NAOJ. We are honored and grateful for the opportunity of observing the Universe from Maunakea, which has the cultural, historical and natural significance in Hawaii.

The Pan-STARRS1 Surveys (PS1) and the PS1 public science archive have been made possible through contributions by the Institute for Astronomy, the University of Hawaii, the Pan-STARRS Project Office, the Max Planck Society and its participating institutes, the Max Planck Institute for Astronomy, Heidelberg, and the Max Planck Institute for Extraterrestrial Physics, Garching, The Johns Hopkins University, Durham University, the University of Edinburgh, the Queen's University Belfast, the Harvard-Smithsonian Center for Astrophysics, the Las Cumbres Observatory Global Telescope Network Incorporated, the National Central University of Taiwan, the Space Telescope Science Institute, the National Aeronautics and Space Administration under grant No. NNX08AR22G issued through the Planetary Science Division of the NASA Science Mission Directorate, the National Science Foundation grant No. AST-1238877, the University of Maryland, Eotvos Lorand University (ELTE), the Los Alamos National Laboratory, and the Gordon and Betty Moore Foundation.

[1] B. Paczynski, Gravitational microlensing by the galactic halo, *The Astrophysical Journal* **304**, 1 (1986).

[2] K. Griest, Galactic microlensing as a method of detecting massive compact halo objects, *The Astrophysical Journal* **366**, 412 (1991).

[3] D. Spergel, N. Gehrels, C. Baltay, D. Bennett, J. Breckinridge, *et al.*, Wide-Field Infrared Survey Telescope-Astrophysics Focused Telescope Assets WFIRST-AFTA 2015 Report, arXiv [10.48550/arxiv.1503.03757](https://arxiv.org/abs/1503.03757) (2015), [1503.03757](https://arxiv.org/abs/1503.03757).

[4] M. T. Penny, B. S. Gaudi, E. Kerins, N. J. Rattenbury, S. Mao, *et al.*, Predictions of the WFIRST Microlensing Survey. I. Bound Planet Detection Rates, *The Astrophysical Journal Supplement Series* **241**, 3 (2019), [1808.02490](https://arxiv.org/abs/1808.02490).

[5] Ž. Ivezić, S. M. Kahn, J. A. Tyson, B. Abel, E. Acosta, *et al.*, LSST: From Science Drivers to Reference Design and Anticipated Data Products, *The Astrophysical Journal* **873**, 111 (2019), [0805.2366](https://arxiv.org/abs/0805.2366).

[6] L. S. Collaboration, P. A. Abell, J. Allison, S. F. Anderson, J. R. Andrew, *et al.*, LSST Science Book, Version 2.0, arXiv [10.48550/arxiv.0912.0201](https://arxiv.org/abs/0912.0201) (2009), [0912.0201](https://arxiv.org/abs/0912.0201).

[7] Y. B. Zeldovich, A Hypothesis, Unifying the Structure and the Entropy of the Universe, *Monthly Notices of the Royal Astronomical Society* **160**, 1P (1972).

[8] S. Hawking, Gravitationally Collapsed Objects of Very Low Mass, *Monthly Notices of the Royal Astronomical Society* **152**, 75 (1971).

[9] B. J. Carr and S. W. Hawking, Black Holes in the Early Universe, *Monthly Notices of the Royal Astronomical Society* **168**, 399 (1974).

[10] B. Carr and F. Kuhnel, Primordial Black Holes as Dark Matter Candidates, arXiv [10.48550/arxiv.2110.02821](https://arxiv.org/abs/2110.02821) (2021), [2110.02821](https://arxiv.org/abs/2110.02821).

[11] A. M. Green and B. J. Kavanagh, Primordial Black Holes as a dark matter candidate, arXiv [10.48550/arxiv.2007.10722](https://arxiv.org/abs/2007.10722) (2020), [2007.10722](https://arxiv.org/abs/2007.10722).

[12] T. M. collaboration, C. Alcock, R. A. Allsman, D. R. Alves, T. S. Axelrod, *et al.*, The MACHO Project: Microlensing Results from 5.7 Years of LMC Observations, *The Astrophysical Journal* **542**, 281 (2000), arXiv: [astro-ph/0001272](https://arxiv.org/abs/astro-ph/0001272), [astro-ph/0001272](https://arxiv.org/abs/astro-ph/0001272).

[13] P. Tisserand, L. L. Guillou, C. Afonso, J. N. Albert, J. Andersen, *et al.*, Limits on the Macho content of the Galactic Halo from the EROS-2 Survey of the Magellanic Clouds ***, *Astronomy & Astrophysics* **469**, 387 (2007), [astro-ph/0607207](https://arxiv.org/abs/astro-ph/0607207).

[14] L. Wyrzykowski, S. Kozłowski, J. Skowron, V. Belokurov, M. C. Smith, *et al.*, The OGLE view of microlensing towards the Magellanic Clouds – II. OGLE-II Small Magellanic Cloud data, *Monthly Notices of the Royal Astronomical Society* **407**, 189 (2010), [1004.5247](https://arxiv.org/abs/1004.5247).

[15] L. Wyrzykowski, Z. Kostrzewska-Rutkowska, J. Skowron, K. A. Rybicki, P. Mróz, *et al.*, Black hole, neutron star and white dwarf candidates from microlensing with OGLE-III, *Monthly Notices of the Royal Astronomical Society* **458**, 3012 (2016), [1509.04899](https://arxiv.org/abs/1509.04899).

[16] A. Udalski, M. K. Szymański, and G. Szymański, OGLE-IV: Fourth Phase of the Optical Gravitational Lensing Experiment, arXiv (2015), [1504.05966](https://arxiv.org/abs/1504.05966).

[17] I. Bond, F. Abe, R. Dodd, J. Hearnshaw, M. Honda, *et al.*, Real-time difference imaging analysis of MOA Galactic bulge observations during 2000, *Monthly Notices of the Royal Astronomical Society* **327**, 868 (2001), [astro-ph/0102181](https://arxiv.org/abs/astro-ph/0102181).

[18] T. Sumi, K. Kamiya, A. Udalski, D. P. Bennett, I. A. Bond, *et al.*, Unbound or Distant Planetary Mass Population Detected by Gravitational Microlensing, *Nature* **473**, 349 (2011), arXiv: [1105.3544](https://arxiv.org/abs/1105.3544), [1105.3544](https://arxiv.org/abs/1105.3544).

[19] H. Niikura, M. Takada, S. Yokoyama, T. Sumi, and S. o. Masaki, Constraints on Earth-mass primordial black holes from OGLE 5-year microlensing events, *Physical Review D* **99**, 083503 (2019), arXiv: [1901.07120](https://arxiv.org/abs/1901.07120), [1901.07120](https://arxiv.org/abs/1901.07120).

[20] P. Mróz, A. Udalski, M. K. Szymański, I. Soszyński, P. Pietrukowicz, *et al.*, Limits on planetary-mass primor-

dial black holes from the OGLE high-cadence survey of the Magellanic Clouds, arXiv 10.48550/arxiv.2410.06251 (2024), 2410.06251.

[21] S. Miyazaki, Y. Komiyama, S. Kawanomoto, Y. Doi, H. Furusawa, *et al.*, Hyper Suprime-Cam: System design and verification of image quality, *Publications of the Astronomical Society of Japan* **70**, S1 (2018).

[22] Y. Komiyama, Y. Obuchi, H. Nakaya, Y. Kamata, S. Kawanomoto, *et al.*, Hyper Suprime-Cam: Camera dewar design, *Publications of the Astronomical Society of Japan* **70**, S2 (2018).

[23] S. Kawanomoto, F. Uraguchi, Y. Komiyama, S. Miyazaki, H. Furusawa, *et al.*, Hyper Suprime-Cam: Filters, *Publications of the Astronomical Society of Japan* **70**, 66 (2018).

[24] H. Furusawa, M. Koike, T. Takata, Y. Okura, H. Miyatake, *et al.*, The on-site quality-assurance system for Hyper Suprime-Cam: OSQAH†, *Publications of the Astronomical Society of Japan* **70**, S3 (2018).

[25] H. Niikura, M. Takada, N. Yasuda, R. H. Lupton, T. Sumi, *et al.*, Microlensing constraints on primordial black holes with the Subaru/HSC Andromeda observation, *Nature Astronomy* **3**, 524 (2019), arXiv: 1701.02151, 1701.02151.

[26] A. P. S. Croots, M31 - A unique laboratory for gravitational microlensing, *The Astrophysical Journal* **399**, L43 (1992).

[27] E. Kerins, B. J. Carr, N. W. Evans, P. Hewett, E. Lastennet, *et al.*, Theory of pixel lensing towards M31 – I. The density contribution and mass of MACHOs, *Monthly Notices of the Royal Astronomical Society* **323**, 13 (2001), astro-ph/0002256.

[28] H. J. Witt and S. Mao, Can lensed stars be regarded as pointlike for microlensing by MACHOs?, *The Astrophysical Journal* **430**, 505 (1994).

[29] A. Gould, Proper Motions of MACHOs, *The Astrophysical Journal* **421**, L71 (1994).

[30] <https://subarutelescope.org/Instruments/HSC/sensitivity.html>.

[31] J. Bosch, R. Armstrong, S. Bickerton, H. Furusawa, H. Ikeda, *et al.*, The Hyper Suprime-Cam software pipeline, *Publications of the Astronomical Society of Japan* **70**, S5 (2018), 1705.06766.

[32] H. Aihara, Y. AlSayyad, M. Ando, R. Armstrong, J. Bosch, *et al.*, Third Data Release of the Hyper Suprime-Cam Subaru Strategic Program, arXiv 10.48550/arxiv.2108.13045 (2021), 2108.13045.

[33] A. Gould, Theory of Pixel Lensing, arXiv 10.48550/arxiv.astro-ph/9509009 (1995), astro-ph/9509009.

[34] C. Alard and R. H. Lupton, A method for optimal image subtraction, arXiv 503, 325 (1997), astro-ph/9712287.

[35] C. Alard, Image subtraction using a space-varying kernel, *Astronomy and Astrophysics Supplement Series* **144**, 363 (2000).

[36] Note that in Niikura *et al.* [25] we used the representative time for the reference image t_{ref} which is defined by the mean time.

[37] <https://github.com/git-sunao/fft-extended-source>.

[38] S. Sugiyama, FFT based evaluation of microlensing magnification with extended source, arXiv 10.48550/arxiv.2203.06637 (2022), 2203.06637.

[39] Note this is not the case in general when we consider the binary lens, parallax, etc.

[40] F. Feroz, M. P. Hobson, and M. Bridges, MultiNest: an efficient and robust Bayesian inference tool for cosmology and particle physics, *Monthly Notices of the Royal Astronomical Society* **398**, 1601 (2009), 0809.3437.

[41] S. Sugiyama, M. Takada, and A. Kusenko, Possible evidence of QCD axion stars in HSC and OGLE microlensing events, arXiv (2021), 2108.03063.

[42] I. Mandel, W. M. Farr, and J. R. Gair, Extracting distribution parameters from multiple uncertain observations with selection biases, *Monthly Notices of the Royal Astronomical Society* **486**, 1086 (2019), 1809.02063.

[43] T. J. Loredo, Accounting for Source Uncertainties in Analyses of Astronomical Survey Data, arXiv 10.48550/arxiv.astro-ph/0409387 (2004), astro-ph/0409387.

[44] R. E. Smith, J. A. Peacock, A. Jenkins, S. D. M. White, C. S. Frenk, *et al.*, Stable clustering, the halo model and nonlinear cosmological power spectra, arXiv 10.48550/arxiv.astro-ph/0207664 (2002), astro-ph/0207664.

[45] P. Mroż, A. Udalski, M. K. Szymański, I. Soszynski, L. Wyrzykowski, *et al.*, No massive black holes in the Milky Way halo, arXiv (2024), 2403.02386.

[46] P. Mroż, A. Udalski, M. K. Szymański, M. Kapusta, I. Soszynski, *et al.*, Microlensing optical depth and event rate toward the Large Magellanic Cloud based on 20 years of OGLE observations, arXiv (2024), 2403.02398.

[47] P. Tisserand, L. L. Guillou, C. Afonso, J. N. Albert, J. Andersen, *et al.*, Limits on the Macho Content of the Galactic Halo from the EROS-2 Survey of the Magellanic Clouds, arXiv 469, 387 (2006), astro-ph/0607207.

[48] M. Oguri, J. M. Diego, N. Kaiser, P. L. Kelly, and T. o. Broadhurst, Understanding caustic crossings in giant arcs: characteristic scales, event rates, and constraints on compact dark matter, arXiv 10.48550/arxiv.1710.00148 (2017), 1710.00148.

[49] T. Blaineau, M. Moniez, C. Afonso, J. N. Albert, R. Ansari, *et al.*, New limits from microlensing on Galactic Black Holes in the mass range $10M_{\odot} < M < 1000M_{\odot}$, arXiv 10.48550/arxiv.2202.13819 (2022), 2202.13819.

[50] B. J. Kavanagh, PBHbounds.

[51] P. Mroż, A. Udalski, J. Skowron, R. Poleski, S. Koźłowski, *et al.*, No large population of unbound or wide-orbit Jupiter-mass planets, *Nature* **548**, 183 (2017), arXiv: 1707.07634, 1707.07634.

[52] C. Han and A. Gould, Stellar Contribution to the Galactic Bulge Microlensing Optical Depth, arXiv 10.48550/arxiv.astro-ph/0303309 (2003), astro-ph/0303309.

[53] N. Smyth, S. Profumo, S. English, T. Jeltema, K. McKinnon, *et al.*, Updated Constraints on Asteroid-Mass Primordial Black Holes as Dark Matter, arXiv 10.48550/arxiv.1910.01285 (2019), 1910.01285.

[54] B. Carr, S. Clesse, J. Garcia-Bellido, M. Hawkins, and F. o. Kuhnel, Observational Evidence for Primordial Black Holes: A Positivist Perspective, arXiv 10.48550/arxiv.2306.03903 (2023), 2306.03903.

[55] A. Kusenko, M. Sasaki, S. Sugiyama, M. Takada, V. Takhistov, *et al.*, Exploring Primordial Black Holes from Multiverse with Optical Telescopes, arXiv:2001.09160 [astro-ph, physics:gr-qc, physics:hep-th] (2020), arXiv: 2001.09160.

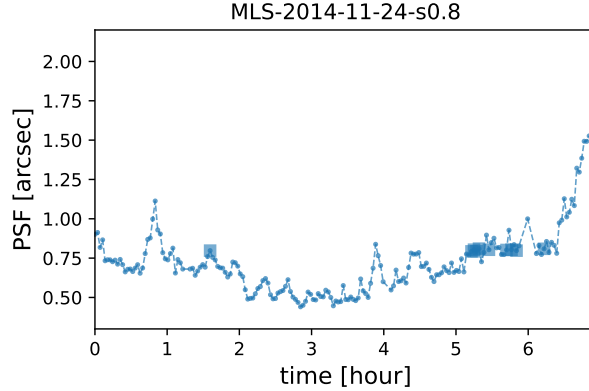


FIG. 9. Same figure as Fig. 1, but with the square data points indicating the 10 images with seeing size $\sim 0.8''$ that are used for making reference images in Appendix A.

TABLE X. The selection process when we use relatively lower-quality images for the reference image. The row names as “2014-11-24” is the fiducial analysis using the best images with smallest seeing size, and identical to the row shown in Table VI. The bottom row named as “2014-11-24-s0.8” is still using the same image data from 2014-11-24, but using the reference image is made by coadding the 10 images whose seeing size is about $0.8''$.

ID	master	bump	mlc2	mlc2i	mlc2o	mlc2il	mlc2ir	mlc2ol	mlc2or	asym	scorr	scorrs	ntscale	amax	mlsig
2014-11-24	7281	5139	1135	938	911	878	819	814	783	391	72	70	57	53	38
2014-11-24-s0.8	5715	5337	1113	963	931	880	837	832	807	289	62	0	0	0	0

Appendix A: Impact of using lower quality reference image

In this appendix, we investigate the impact of using lower-quality images to construct the reference image. For comparison with the best-performing scenario, we use data from 2014-11-24, which have the highest image quality and the smallest seeing values.

We select 10 images with seeing sizes of approximately $0.8''$ and create a lower-quality reference image by coadding them. The seeing of the images used for this experiment are indicated in Fig. 9. We then obtain difference images by subtracting this lower-quality reference image from each individual image. Image-level detection and photometric measurements are performed on these difference images to produce another master catalog. Finally, we apply the same selection criteria as in the main analysis described in Section III to the master catalog to identify microlensing candidates. The results are summarized in Table X, together with those from the fiducial analysis for ease of comparison. After applying all selection criteria, no events remain. This result indicates that the high quality of the reference image is crucial for the efficient detection of microlensing events.

Appendix B: Event rate and event number

We start defining the differential event rate by following Niikura *et al.* [25]. We define the differential eventrate with respect to four variables: the distance to the lens object d , the event time scale \hat{t} , the angle to enter the Einstein circle θ on the sky, and the physical source radius R_s . We group the part of variables as $\boldsymbol{\theta} = \{\hat{t}, \theta, R_s\}$ for the later purpose. The differential eventrate is

$$\frac{d\Gamma}{d\hat{t} d\theta dR_s} = f(R_s) \sum_{h \in \text{M31, MW}} \frac{\rho_{\text{DM},h}(d)v_{c,h}^2}{M_{\text{PBH}}} \left(\frac{v_r}{v_{c,h}} \right)^4 \exp \left[-\frac{v_r^2}{v_{c,h}^2} \right] \quad (\text{B1})$$

where $\rho_{\text{DM},h}$ and $v_{c,h}$ are the mass profile and the velocity dispersion of the h -th galaxy halo, which is either of Milky Way (MW) or M31 galaxy. The velocity realization of the lens object that belongs to h -th galaxy halo is defined as $v_r = 2R_E u_T(\rho) \cos \theta / \hat{t}$ where $\rho = \theta_s / \theta_E = (R_s/d_s) / (R_E/d)$ is the source size radius in the unit of Einstein radius on the lens plane, and u_T is the minimum impact parameter within which the magnification becomes a certain threshold ($A = 1.34$). We introduced the distribution of the background source sizes $f_s(R_s)$ with R_s a physical size of the source radius. We use the source-size distribution estimated in Smyth *et al.* [53], and normalize it such that $\int dR_s f_s(R_s) = 1$.

To obtain the differential eventrate only for \hat{t} , we can integrate over all other variables,

$$\frac{d\Gamma}{d\hat{t}} = \int_0^{d_s} dd \int_0^\infty dR_s \int_{-\pi/2}^{\pi/2} d\theta \frac{d\Gamma}{ddd\boldsymbol{\theta}'} \quad (\text{B2})$$

The integral over θ can be analytically performed to reduce the expression to

$$\frac{d\Gamma}{d\hat{t}} = \sum_h \int_0^{d_s} dd \int_0^\infty dR_s f_s(R_s) \frac{\rho_{\text{DM},h}(d)v_{c,h}^2}{M_{\text{PBH}}} I\left(\frac{2R_E u_T}{v_{c,h} \hat{t}}\right) \quad (\text{B3})$$

$I(x) = \pi/2 x^2 e^{-x^2/2} [x^2 I_0(x^2/2) - (1+x^2) I_1(x^2/2)]$ with $I_{0,1}$ the first kind of modified Bessel function of zero and first order.

By integrating over the event time scale, accounting for the efficiency, we obtain the event rate for n -th night

$$\Gamma_n = \int_0^\infty d\hat{t} \epsilon_{\text{eff},n}(\hat{t}) \frac{d\Gamma}{d\hat{t}} \quad (\text{B4})$$

where $\epsilon_{\text{eff},n}$ is the effective detection efficiency introduced in Eq. (13), accounting for the magnitude dependence of the efficiency and the numbers of source stars in different magnitude bins.

The number of events for the n -th night is then obtained by

$$N_{\text{exp},n} = N_{\text{tot}} T_{\text{eff},n} \Gamma_n. \quad (\text{B5})$$

The total number of the events for whole observations can be simply obtained by summing the expected number of events for each observation date; $N_{\text{exp,tot}} = \sum_n N_{\text{exp},n}$.

Appendix C: Light curves

In this appendix, we present the light curves of the events in the candidate catalog selected from master catalog in Section III C. Fig. 10 shows the light curves together with the theoretical prediction of PLFS model using the best-fit parameters of light curve fitting.

Appendix D: Posteriors of light-curve fitting for selected events

In this appendix, we present the posterior distribution of the model parameters for each selected light-curve in Section III C. We only shows the 1D/2D marginalized posterior for ρ, u_0, t_E , and a derived parameter \hat{t} . We found that the parameter degeneracy is strong for ρ, u_0, t_E for most of the events, and \hat{t} has bounded posterior distribution with less degeneracy than others. This motivates the use of \hat{t} as a nominal time scale parameter of each event.

Appendix E: Lightcurve likelihood for hierarchical Bayesian inference

In this appendix, we explain how to perform the integral in the denominator of in Eq. (18). Here, we only consider one light curve data \mathbf{d}_j^n , but the same applies to other light curve data to construct the likelihood for a set of observed light curves.

As is discussed in Mandel *et al.* [42], the likelihood can be rewritten in terms of the posterior of the PLFS parameters for a given light curve data,

$$\int dd \int d\boldsymbol{\theta} P(\mathbf{d}_j^n | \boldsymbol{\theta}) \frac{d\Gamma}{ddd\boldsymbol{\theta}}(\boldsymbol{\lambda}) = P(\mathbf{d}_j^n) \int dd \int d\boldsymbol{\theta} \frac{P(\boldsymbol{\theta} | \mathbf{d}_j^n)}{\Pi(\boldsymbol{\theta})} \frac{d\Gamma}{ddd\boldsymbol{\theta}}(\boldsymbol{\lambda}) \quad (\text{E1})$$

where $P(\mathbf{d}_j^n)$ is the data evidence and $\Pi(\boldsymbol{\theta})$ is the parameter prior used in the analysis (see Table V for our PLFS case). We used flat prior for the PLFS parameters for the parameter inference, and therefore we can effectively neglect the effect of the prior as far as we keep the integral variable to be $\boldsymbol{\theta} = \{t_E, u_0, \rho\}$. We also omit $P(\mathbf{d}_j^n)$, because it only gives constant factor and does not depends on the population parameter $\boldsymbol{\lambda}$.

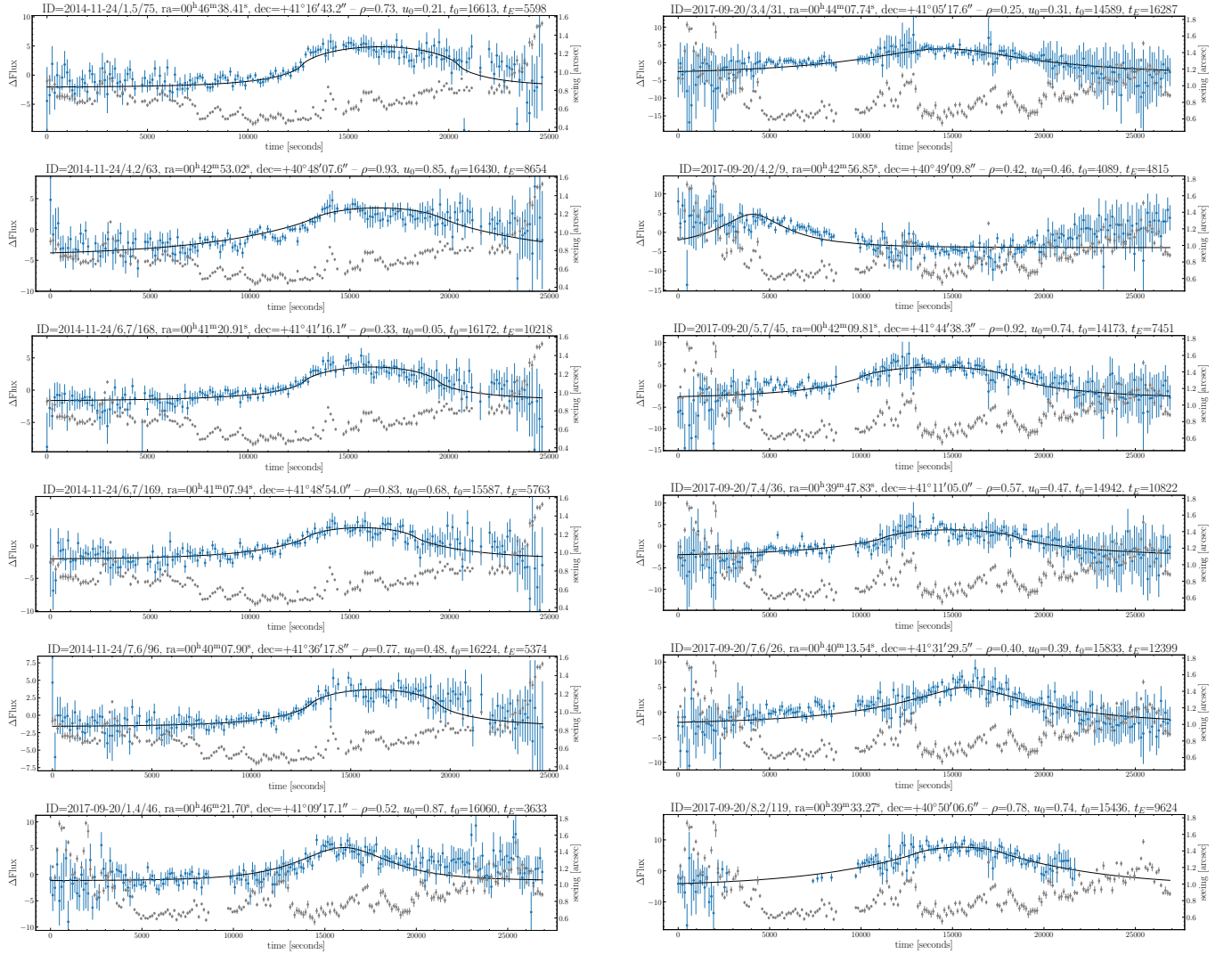


FIG. 10. Light curves of the 12 selected events in the candidate catalog the property of these events are summarized in Table VII. The blue data points are the flux data points obtained by the forced photometry on the detection point on the difference image. The black curve is the theoretical prediction by the microlensing PLFS model with the best-fit parameters of light curve fitting.

We wish to substitute the differential eventrate introduced in Eq. (B1) into the above expression. However, the differential eventrate in Appendix B is a function of $\boldsymbol{\theta}' = \{\hat{t}, \theta, R_s\}$, so we need to account for the Jacobian, which is

$$\frac{d\Gamma}{d\boldsymbol{\theta}} = \frac{\partial \boldsymbol{\theta}'}{\partial \boldsymbol{\theta}} \frac{d\Gamma}{d\boldsymbol{\theta}'} \equiv J \frac{d\Gamma}{d\boldsymbol{\theta}'} \quad (E2)$$

The variable $\boldsymbol{\theta}'$ can be written in terms of $\boldsymbol{\theta}$ as

$$\begin{cases} \hat{t} &= 2t_E \sqrt{u_T^2(\rho) - u_0^2} \\ R_s &= \rho d_s \theta_E \\ \theta &= \arccos\left(\frac{u_0}{u_T}\right) \end{cases} \quad (E3)$$

We can easily find that the Jacobian matrix is a triangle matrix (after appropriate permutation of variables), and therefore the determinant of the Jacobian matrix becomes as simple as

$$|J| = \left| \frac{\partial \hat{t}}{\partial t_E} \right| \left| \frac{\partial R_s}{\partial \rho} \right| \left| \frac{\partial \theta}{\partial u_0} \right| = 2d_s \theta_E \quad (E4)$$

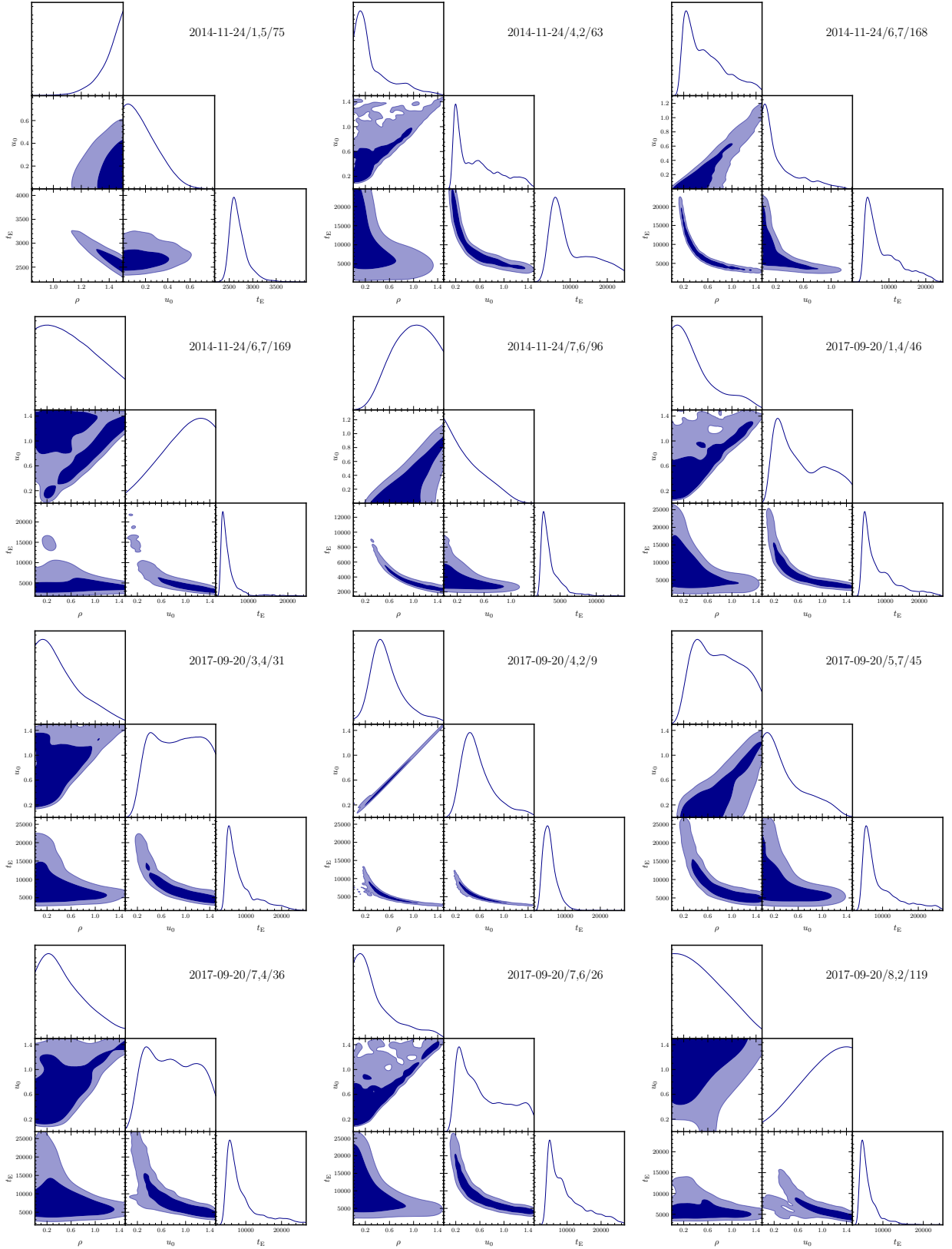


FIG. 11. Posteriors of the PLFS parameters, $\boldsymbol{\theta} = (\rho, u_0, t_E, \hat{t})$ for the events in the candidate catalog. The first five panels show the posteriors for events of 2014-11-24, and the rest for 2017-09-20 data.

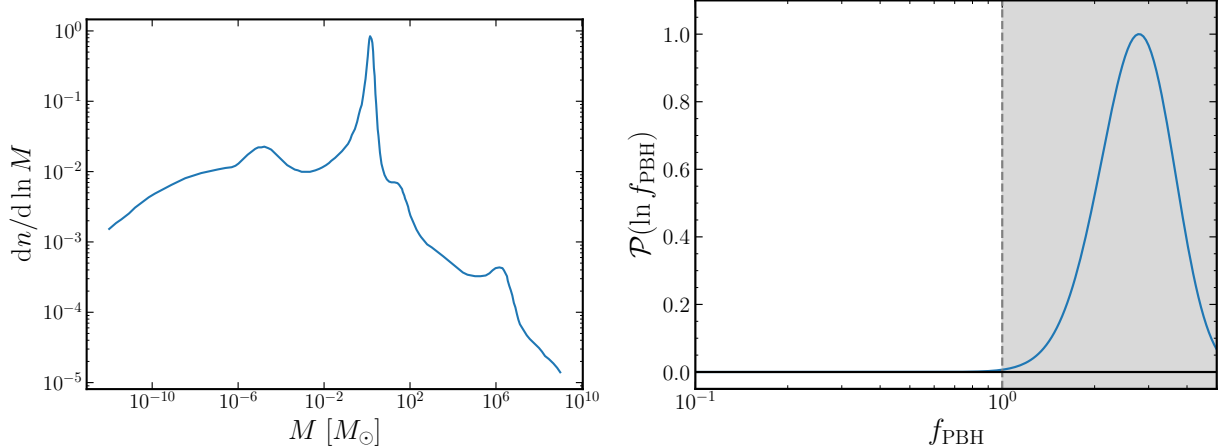


FIG. 12. *Left:* The shape of the extended mass function proposed by Carr *et al.* [54]. *Right:* The posterior distribution of the amplitude of the mass function, obtained by using the secure events of this work.

Including the Jacobin determinant appropriately, we obtain the numerator of the light-curve likelihood as

$$\int d\theta \int d\theta P(\theta | d_j^n) |J| \frac{d\Gamma}{d\theta d\theta'}(\lambda) = \sum_h \int dd \frac{\rho_{\text{DM},h}(d) v_{c,h}^2(d)}{M_{\text{PBH}}} \frac{d_s R_E}{d} \int d\theta P(\theta | d_j^n) f_s(R_s) \left(\frac{v_r}{v_{c,h}} \right)^4 \exp \left[- \left(\frac{v_r}{v_{c,h}} \right)^2 \right] \quad (\text{E5})$$

where R_s and v_r are now defined as functions of θ ; $R_s(\theta)$ depends on ρ as in Eq. (E3), and $v_r(\theta) = R_E/t_E$, and we omit the dependence on d and M_{PBH} for simplicity of notation now. We evaluate the above θ integral by Monte-Carlo integration using the samples of PLFS parameter set θ obtained from the light curve fitting in Section III D.

$$\sum_h \int dd \frac{\rho_{\text{DM},h}(d) v_{c,h}^2(d)}{M_{\text{PBH}}} \frac{d_s R_E}{d} \sum_{q \in \text{MC chain}} f_s(R_s(\theta_q)) \left(\frac{v_r(\theta_q)}{v_{c,h}} \right)^4 \exp \left[- \left(\frac{v_r(\theta_q)}{v_{c,h}} \right)^2 \right] \quad (\text{E6})$$

Note that we do not have $P(\theta | d_j^n)$ in the above equation because the samples to evaluate the integral follow the probability density already. We appropriately include the weights of the MC samples, because our samples are obtained by a nested sampler `MultiNest` [40], which provides the weights of the samples.

Appendix F: Testing some extended mass function of PBH

In this appendix, we present some example tests of the PBH mass function that have more extended shape in mass function. As the first test example, we consider the model by Carr *et al.* [54]. The shape of the mass function is motivated by some candidate of positive signals of the PBH from various observations, and its mass function shape is shown in Fig. 12.

To test this model, we introduce a free parameter, the overall amplitude of abundance f_{PBH} , while fixing the spectrum shape of the mass function. We infer the amplitude using the secure events by following the method in Section V. The resultant posterior distribution of f_{PBH} is shown in Fig. 12, where we see that the HSC result prefers $f_{\text{PBH}} > 1$, which indicates that the mass function has too small amplitude at the mass scale to explain the HSC secure events.

Nest, we consider the mass function predicted by Kusenko *et al.* [55]. The mass function has the following functional form

$$\frac{dn}{d \ln M} \propto \begin{cases} 0 & (M < M_{\text{min}}) \\ (M/M_{\text{min}})^{-1/2} & (M_{\text{min}} < M < M_1) \\ (M_1/M_{\text{min}})^{-1/2} & (M_1 < M < M_2) \\ (M_1/M_{\text{min}})^{-1/2} (M/M_2)^{-1/2} & (M_2 < M) \end{cases} \quad (\text{F1})$$

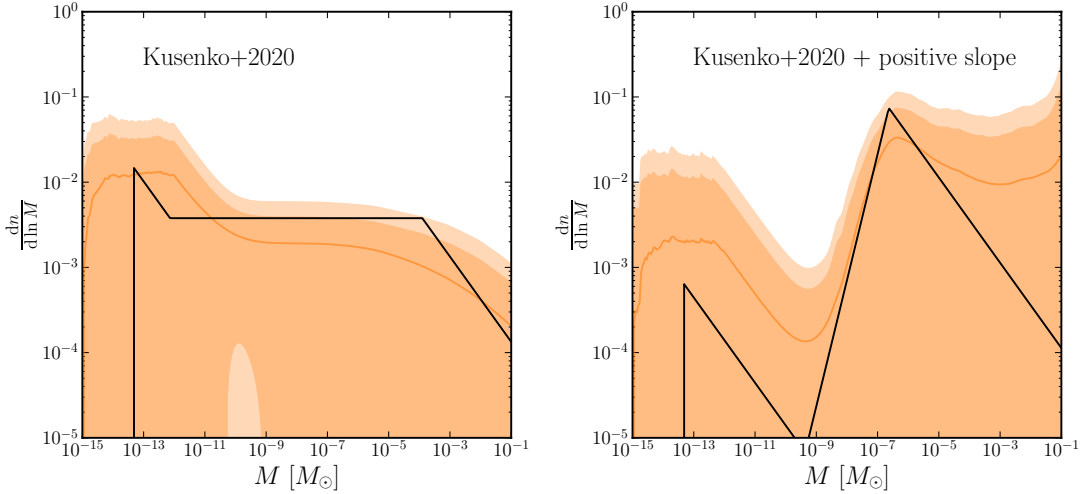


FIG. 13. The posterior distribution of the extended mass function proposed in Kusenko *et al.* [55]. *Left*: The light- and dark-shaded region is the 68% and 95% credible distribution of the extended mass function obtained using the posterior samples of the model parameters of Eq. (F1). The reason why the mass function is smooth instead of step like is the step-like mass functions are averaged over for various model parameters in the posterior. The black lines are the the mass function obtained by using the best-fit model in the posterior samples. *Right*: The similar figure as the left, but the model with an additional free parameter allowing positive slope in the intermediate mass scale.

with M_1 and M_2 free parameters associated with the beginning and the end time of the intermediate matter dominated era in the early Universe.

Fig. 13 shows the constraint on the mass function. We notice that although we have a non-zero events in the PBH hypothesis, the overall amplitude is strongly suppressed. This is because, even in the PBH hypothesis, the PBH mass function is allowed to be abundant only at the mass scale of $10^{-7} M_\odot$ and the smaller abundance is preferred at the lower mass scale. For this model, the mass function is extended broadly over the various mass scale, and its shape is fixed in the mass scale of HSC sensitivity, and therefore these effects compete, and as a consequence the smaller total abundance is preferred.

Although it is not motivated by the theory, we introduce an additional free parameter in this model to understand how the constraint changes when we change the shape of the mass function in the HSC sensitivity scales,

$$\frac{dn}{d \ln M} \propto \begin{cases} 0 & (M < M_{\min}) \\ (M/M_{\min})^{-1/2} & (M_{\min} < M < M_1) \\ (M_1/M_{\min})^{-1/2}(M/M_1)^p & (M_1 < M < M_2) \\ (M_1/M_{\min})^{-1/2}(M_2/M_1)^p(M/M_2)^{-1/2} & (M_2 < M) \end{cases} \quad (\text{F2})$$

where we allow a positive slope in the mass function for $M_1 < M < M_2$. The constraint on this mass function is shown in Fig. 13. We see that indeed the positive slope is preferred, which is because the abundant PBH is only allowed at the mass scale $M \sim 10^{-7} M_\odot$ and lower abundance is preferred at the lower mass scale, leading highest peak at $M \sim 10^{-7} M_\odot$.